

1
2
3
4
5
6
7
8
9
10
11
12
13
14
15
16
17
18
19
20
21

Reduced Rainfall in Future Heavy Precipitation Events Related to Contracted Rain Area Despite Increased Rain Rate

Moshe Armon¹, Francesco Marra², Yehouda Enzel¹, Dorita Rostkier-Edelstein^{1,3}, Chaim I. Garfinkel¹, Ori Adam¹, Uri Dayan⁴, Efrat Morin¹

¹Fredy and Nadine Herrmann Institute of Earth Sciences, the Hebrew University of Jerusalem, Jerusalem, 9190401, Israel

²National Research Council of Italy, Institute of Atmospheric Sciences and Climate, CNR-ISAC, Bologna 40129, Italy.

³Department of Environmental Physics, Environmental Sciences Division, IIBR, Ness-Ziona 7410001, Israel.

⁴Department of Geography, the Hebrew University of Jerusalem, Jerusalem, 9190401, Israel.

Corresponding author: Moshe Armon (moshe.armon@mail.huji.ac.il)

Key Points:

- End of 21st century heavy precipitation events in the eastern Mediterranean are projected to have substantially reduced rainfall yield
- This reduction results mainly from a major decrease in rain area during future events, despite the increased conditional rain rate
- Changes in rain yield, rate, and area are consistent across many events, suggesting great hydrological implications for the region

22 **Abstract**

23 Heavy precipitation events (HPEs) can lead to deadly and costly natural disasters and are critical
24 to the hydrological budget in regions where rainfall variability is high and water resources
25 depend on individual storms. Thus, reliable projections of such events in the future are needed.
26 To provide high-resolution projections under the RCP8.5 scenario for HPEs at the end of the 21st
27 century and to understand the changes in sub-hourly to daily rainfall patterns, weather research
28 and forecasting (WRF) model simulations of 41 historic HPEs in the eastern Mediterranean are
29 compared with “pseudo global warming” simulations of the same events. This paper presents the
30 changes in rainfall patterns in future storms, decomposed into storms’ mean conditional rain rate,
31 duration, and area. A major decrease in rainfall accumulation (-30% averaged across events) is
32 found throughout future HPEs. This decrease results from a substantial reduction of the rain area
33 of storms (-40%) and occurs despite an increase in the mean conditional rain intensity (+15%).
34 The duration of the HPEs decreases (-9%) in future simulations. Regionally maximal 10-min rain
35 rates increase (+22%), whereas over most of the region, long-duration rain rates decrease. The
36 consistency of results across events, driven by varying synoptic conditions, suggests that these
37 changes have low sensitivity to the specific large-scale flow during the events. Future HPEs in
38 the eastern Mediterranean will therefore likely be drier and more spatiotemporally concentrated,
39 with substantial implications on hydrological outcomes of storms.

40 **Plain Language Summary**

41 Heavy precipitation events are large storms that can recharge freshwater reservoirs, but can also
42 lead to hazardous outcomes such as flash floods. Therefore, understanding the impacts of climate
43 change on such storms is critical. Here, a weather model similar to those used in weather
44 forecasts is used to simulate heavy precipitation events in the eastern Mediterranean. A large
45 collection of storms is simulated in pairs: (1) historic storms, known for their high impact, and
46 (2) placing the same storms in a global warming scenario projected for the end of the 21st
47 century. Using these simulations we ask how present-day storms would look like were they to
48 occur at the warmer end of the 21st century. The future storms are found to produce much less
49 rainfall compared to the historic ones. This decrease in rainfall is attributed mainly to the
50 reduction in the area covered by storms’ rainfall, and happens despite increasing rainfall
51 intensities. These results suggest that the region will be drier in the future with larger dry areas
52 during storms; however, over short durations, it would rain more intensely over contracted areas
53 – increasing local hazards associated with heavy precipitation events.

54 **1 Introduction**

55 Expected impacts of climate change on rainfall during heavy precipitation events (HPEs)
56 have the potential to significantly alter their influence on future societies. Where precipitation
57 variability is high, such as in Mediterranean and arid climates, the impact of individual HPEs in
58 terms of both peril (e.g., Borga et al., 2014; Dayan et al., 2021; Raveh-Rubin & Wernli, 2016;
59 Rinat et al., 2020; De Vries et al., 2013) and water resources (Flaounas et al., 2021; Nasta et al.,
60 2018; Samuels et al., 2009; R. G. Taylor et al., 2013) is great, and reliable projections of HPEs
61 are needed (e.g., Sillmann et al., 2021).

62 Individual HPEs are controlled by specific large scale and synoptic circulation patterns.
63 However, projected changes in the atmospheric circulation are highly uncertain across global
64 climate models (GCMs) due to the wide variety of factors at play (Shepherd, 2014).

65 Furthermore, climate change impact on HPEs can be quite different from the well-studied impact
66 on the mean rainfall or even on high precipitation percentiles (e.g., Donat et al., 2016; Kendon et
67 al., 2018; Moustakis et al., 2021; O’Gorman, 2015; Pfahl et al., 2017; Trenberth et al., 2015).

68 Detailed projections of the regional rainfall during a specific event can only be provided
69 by models that can explicitly resolve the convective processes governing precipitation during
70 HPEs (e.g., Fosser et al., 2014). Indeed, convection-permitting models (CPMs) are more reliable
71 than GCMs in simulating spatiotemporal precipitation patterns (Ban et al., 2014; Cannon &
72 Innocenti, 2019; Crook et al., 2019; Kendon et al., 2014; Meredith et al., 2020; Poujol et al.,
73 2020; Prein et al., 2015, 2017; Westra et al., 2014). Recent methodological and computing
74 advances enable “climate” CPM simulations with long-term (~10 yr), large-scale (continental),
75 and high resolution (a few kilometers) outputs with some groups already running ensemble
76 simulations over specific regions (Chan et al., 2020; Coppola et al., 2020; Pichelli et al., 2021).
77 These give probabilistic projections of changes in precipitation extremes with expectations to
78 achieve better quantification of future HPEs (e.g., Kendon et al., 2014; Poujol et al., 2020).
79 However, rare extreme or heavy precipitation events are, by definition, hard to assess even with
80 such simulations (e.g., Fatichi et al., 2016; Kendon et al., 2021). Moreover, a few kilometers
81 resolution may still not be sufficient to represent the local nature of convective clouds, especially
82 when shallow convection is present (Kendon et al., 2021; Prein et al., 2015). Therefore, trying to
83 provide reliable projections of the changes in rainfall patterns during HPEs will probably take
84 many more years of improvement in climate modeling. A complementing approach, aimed at
85 resolving extreme events and intra-event characteristics (Fowler, Ali, et al., 2021; O’Gorman,
86 2015), is to provide projections of specific high impact events either by identifying interesting
87 events such as hurricanes over long-term simulations (Gutmann et al., 2018), or through the
88 simulation of individual events known for their high-impact, such as snowstorms (G. Chen et al.,
89 2020), tropical cyclones (J. Chen et al., 2020), or HPEs (Ferreira, 2021).

90 Pseudo global warming (PGW) is an emerging methodology for event-based projections,
91 enabling assessment of the impacts of one or more meteorological parameters over local-scale
92 weather events (Brogli et al., 2019; Fowler, Lenderink, et al., 2021; Moustakis et al., 2021; Prein
93 et al., 2017; Sato et al., 2007; Schär et al., 1996). The PGW methodology imposes a certain
94 climate change, e.g., temperature rise, over the initial and boundary conditions of a regional
95 model, by prescribing the synoptic and larger-scale changes from GCMs, while allowing smaller
96 scale features to develop freely within a downscaled modeled domain in a physically consistent
97 manner. Further, projections of precipitation extremes under global warming scenarios
98 commonly focus on daily resolutions (Donat et al., 2016; O’Gorman, 2015; Pfahl et al., 2017),
99 which hinders the possible impact of short-duration extremes; only recently more studies have
100 directed attention to changes expected over sub-daily or even sub-hourly extremes (Fowler, Ali,
101 et al., 2021; Fowler, Wasko, et al., 2021; Morrison et al., 2019). However, to understand the
102 potential effects of changes in precipitation extremes, not only their changing intensity and
103 frequency are important, but also high-resolution changes in intra-event characteristics, such as
104 the spatiotemporal organization of the storms (Li et al., 2018). This requires high-resolution
105 analysis of many high-impact storms of different synoptic-scale circulations, as there is no
106 guarantee that different HPEs behave the same way (Fowler, Ali, et al., 2021).

107 The goal of this study is to identify and quantify changes in rainfall patterns during HPEs
108 induced by global warming, and to examine whether a common change emerges over a variety of
109 HPEs. To do so, we exploit the case of the eastern Mediterranean (Sect. 2.1) to simulate a large

110 number of HPEs using the PGW methodology with a very high spatiotemporal resolution, and
111 explicitly consider space-time patterns of rainfall during the events over durations of 10-min to
112 24-h.

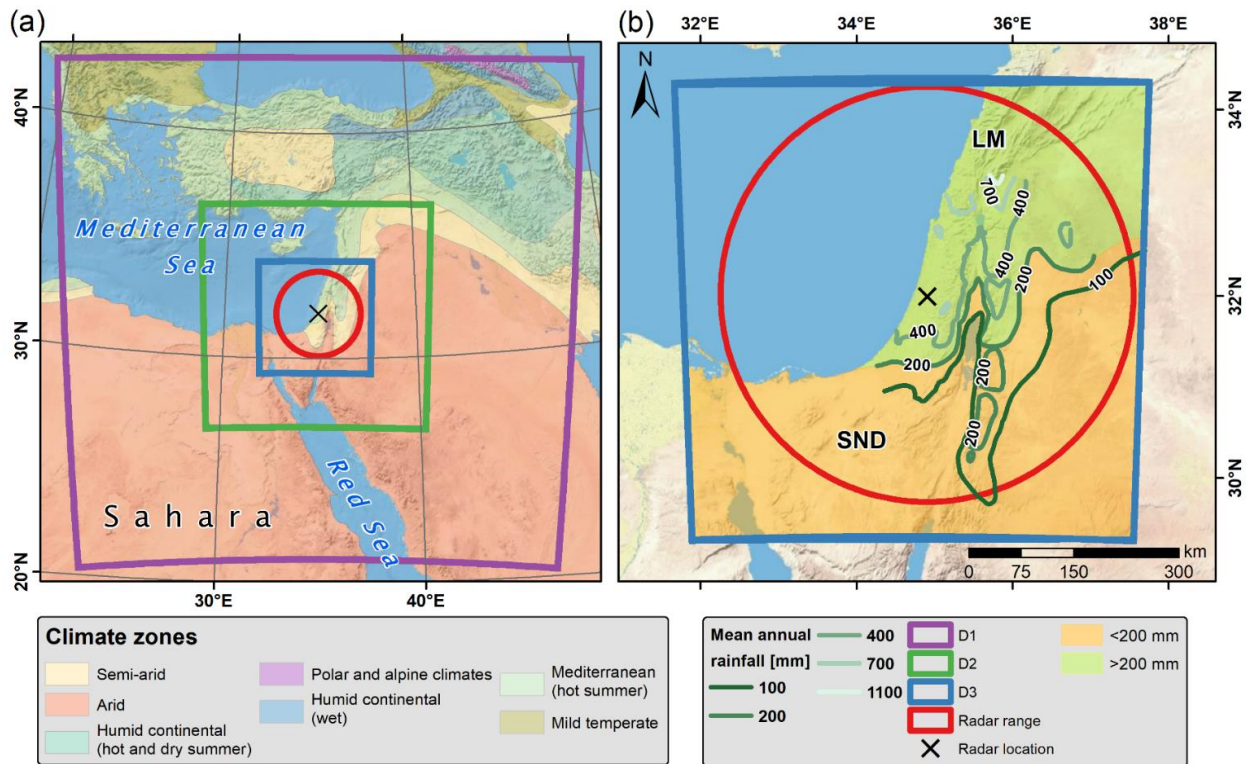
113 The paper is organized as follows: Section 2 describes the study region and outlines the
114 modeling strategy and the analyses of rainfall patterns. We first demonstrate the expected
115 changes for a specific HPE case (Sect. 3.1), and then examine changes in rainfall accumulation
116 over a large set of HPEs (Sect. 3.2). Changes in specific rainfall properties are outlined in Sect.
117 3.2-3.4, with the unique role of the rain area shown in Sect. 3.3.1. Section 4 begins with a
118 discussion of the event-based approach (Sect. 4.1) and continues with an examination of the
119 change in rainfall patterns in future HPEs (Sect. 4.2). Our conclusions are presented in Sect. 5.

120 **2 Study Region, Data, and Methods**

121 **2.1 Study Region**

122 The focus here is on the eastern Mediterranean (Fig. 1), which (a) is expected to suffer
123 from a large future decrease in total rainfall (Garfinkel et al., 2020; Giorgi & Lionello, 2008;
124 Zappa et al., 2015), (b) may experience an increase in extreme precipitation occurrence (Alpert
125 et al., 2002; Marra et al., 2021; Samuels et al., 2017), (c) is characterized by the least
126 precipitation per capita in the world (Dirmeyer et al., 2009), and (d) is exposed to large rainfall
127 variability (Morin, 2011). These characteristics result in a large dependency on HPEs, in terms of
128 water resources and vulnerability to natural hazards; therefore, we explore here possible future
129 changes in HPEs in the region, and disassemble them to their distinct hydrometeorological
130 constituents. It is important to note there is currently no CPM with future projections available
131 for the study region.

132 In the eastern Mediterranean (Fig. 1a), the Mediterranean climate abuts the semiarid to
133 hyperarid climates characterizing the region to the south and east of the Mediterranean Sea.
134 Yearly rainfall amounts drop from >1000 mm in the northern mountains, to <<100 mm at the
135 southeast regions (Fig 1b). Summers are dry, and the rainy season is October to May, with a few
136 rare exceptions in September and June (Yair Goldreich, 2012; Kushnir et al., 2017). The core of
137 the rainy season is December-February (>65% of precipitation). However, the rainy season's
138 midpoint changes from the beginning of January near the Mediterranean Sea to the end of
139 January farther inland (Y. Goldreich, 1994; Yair Goldreich, 1995). This reflects the important
140 contribution of the warm Mediterranean Sea water to building up of Mediterranean Cyclones
141 (MCs), the favorable synoptic condition prevailing during rainy days, generating >90% of all
142 rainfall in the northern, wetter part of the region (Alpert & Shay-EL, 1994; El-Fandy, 1946; Ziv
143 et al., 2006). Other synoptic systems contribute relatively large rain amounts to the interior-
144 desert area mainly during the transitional seasons (Armon et al., 2019; Dayan & Morin, 2006;
145 Kahana et al., 2002), including the more frequent (a) active Red Sea troughs (ARSTs) (Ashbel,
146 1938; De Vries et al., 2013), occurring mainly in fall, and (b) less frequent disturbances in the
147 Subtropical Jet sometimes termed Tropical Plumes or Active Subtropical Jet (Armon et al., 2018;
148 Dayan & Abramski, 1983; Rubin et al., 2007; Tubi et al., 2017).



149

150 **Figure 1.** Map of the study area. (a) Köppen-Geiger climate classification of the eastern
 151 Mediterranean (Atlas of Israel, 2011), weather research and forecasting (WRF) model domains
 152 (D1-D3; Sect. 2.3), and the range of the weather radar used for the identification of events (Sect.
 153 2.2). (b) Mean annual rainfall based on 1960-1990 interpolated rain gauge data (Enzel et al.,
 154 2003), the innermost model domain, and the weather radar range. Green and yellow colors,
 155 corresponding to drier and wetter than 200 mm yr⁻¹, respectively, roughly mark the extent of the
 156 desert and Mediterranean climate regions. SND = Sinai-Negev Desert, LM = Lebanon
 157 Mountains.

158

2.2 HPEs Identification

159

A collection of carefully selected HPEs was used in this study (Table S1 in the
 160 Supporting Information) following Armon et al. (2020) and described here briefly. It consists of
 161 41 HPEs identified based on their magnitude compared to a 24-year rainfall climatology from
 162 physically-corrected and gauge-adjusted weather radar rainfall data (Marra & Morin, 2015; Fig.
 163 1b). A HPE was identified when at least a thousand 1-km² radar pixels exhibited a rain amount
 164 greater than the local 99.5th quantile of the non-zero amounts for multiple durations, thus
 165 revealing events which can be considered locally intense. To have a good representation of both
 166 short- and long-duration HPEs, this process was repeated for durations of 1-72 h. Events
 167 identified as a HPE for more than one duration were merged (Table S1). Return levels of the
 168 99.5th quantile thresholds are roughly 2-10 years. Events were separated by at least 24 h with less
 169 than 100 pixels displaying rainfall of more than 0.1 mm, and they span 3.4 ± 1.6 d (mean and
 170 standard deviation). This collection of HPEs represents a large variance of synoptic conditions,
 171 associated with both MCs (35 events) and ARSTs (six events). A detailed description of the
 172 collection of events and their rainfall characteristics is given in Armon et al. (2020).

173 2.3 WRF Simulations

174 Each of the 41 HPEs was simulated twice, using version 3.9.1.1 of the weather research
175 and forecasting (WRF) model, at a convection permitting resolution. The first simulation of each
176 event represents the historic conditions during the storm (near the end of the 20th century; sect.
177 2.3.1). Results of these simulations were previously published (Armon et al., 2020). The second
178 simulation represents a hypothetical storyline in which the same HPE hits the area by the end of
179 the 21st century, when global warming conditions at a representative concentration pathway
180 (RCP) 8.5 prevail in the region (sect. 2.3.2).

181 2.3.1 Simulation of Historic HPEs

182 Simulation of historic HPEs was conducted at a configuration suitable for a skillful
183 representation of rainfall patterns in the eastern Mediterranean (Armon et al., 2020; Romine et
184 al., 2013; Rostkier-Edelstein et al., 2014; Schwartz et al., 2015). This configuration includes
185 three two-way nested domains (Fig. 1a; Table S2) in which the innermost domain is simulated at
186 a very high spatial and temporal resolution (1 km², 4-8 s). Convective parametrization was used
187 only in the two outer nests, while in the inner nest the resolution is high enough to explicitly
188 represent convection (e.g. Prein et al., 2015). Further details are described in Table S2 and in
189 Armon et al. (2020).

190 Initial and boundary conditions for the historic simulations are 6-hourly ERA-Interim
191 reanalysis data, at 60 vertical layers with a T255 spectral spatial resolution (~80 km) (Dee et al.,
192 2011). HPEs were simulated starting 24 h before the beginning of the observed rainfall (rounded
193 down to the previous 6 h) and lasted until the end of the HPE (rounded to the following 6 h). The
194 24 h period before the event is considered a spinup phase, for which we discard the rain fields.
195 This duration is considered long enough to correct spatial heterogeneities arising from the initial
196 conditions (Gómez-Navarro et al., 2019; Picard & Mass, 2017; Warner, 2011: pp 215-216),
197 which is crucial in correcting non-physical properties of the atmosphere, expected to be present
198 in the PGW simulations because of the usage of ensemble mean fields (Shepherd, 2019; Tebaldi
199 & Knutti, 2007) (Sect. 2.3.2). Precipitation outputs for the innermost domain were saved at 10
200 min intervals.

201 As was shown by Armon et al. (2020), the total precipitation during most of the HPEs
202 reproduces the structure, location, and the seasonal change of the precipitation's center-of-mass
203 of radar-observed precipitation, albeit with a positive bias. Given that HPEs in the region are
204 characterized by small spatiotemporal scale rain-cells, it is important to note the model's skill is
205 particularly good at its "raw" (1 km²) resolution for total rain amounts of <25 mm, however, for
206 larger amounts a skillful representation must include a spatial averaging of at least a few tens of
207 square kilometers. The model also well represents areal mean rainfall amounts, for various
208 durations, which are crucial drivers of the hydrological response to precipitation. MC-type HPEs
209 are better simulated compared to ARSTs, which are in general shorter and more local in nature.

210 2.3.2 Simulation of "Future" HPEs

211 To simulate the occurrence of the same HPEs in the future we used the "pseudo global
212 warming" (PGW) methodology (Kawase et al., 2009; Rasmussen et al., 2011; Schär et al., 1996).
213 Each of the simulated HPEs was forced with the same input data as the historic events (Sect.
214 2.3.1) after adding the signal of climate change to the following input variables: surface pressure,
215 skin temperature (including sea surface temperature), and 3D fields of temperature, wind, and

216 specific humidity. In contrast to homogeneous changes common in the surrogate climate-change
 217 methodology (Keller et al., 2018; Schär et al., 1996), 3D spatial heterogeneity in the altered
 218 fields used in PGW experiments allows for representation of non-uniform spatial response to
 219 global warming (e.g., Rasmussen et al., 2011).

220 The changes applied over the initial and boundary conditions, for each pixel and timestep
 221 (denoted hereon as Δ), were derived from the monthly values (Oct-Apr) of the ensemble mean of
 222 29 models of the Coupled Model Intercomparison Project phase 5 (CMIP5; Table S3) (K. E.
 223 Taylor et al., 2012). They were based on the difference in the corresponding parameter values for
 224 the end of the 21st century and the end of the 20th century under an RCP 8.5 scenario, as follows:

$$225 \quad \Delta X_j = \overline{\overline{X_j}}_{2074-2099}^{29 \text{ models}} - \overline{\overline{X_j}}_{1979-2004}^{29 \text{ models}}, \quad (1)$$

226 where X is a specified meteorological variable, defined for the particular month (j) of the HPE
 227 occurrence. The double overbar represents the mean of this parameter over the future (2074 to
 228 2099) or historic (1979 to 2004) periods, averaged among the 29 CMIP5 models. Δ fields were
 229 linearly interpolated into a common grid, similar to the ERA-Interim horizontal grid (T255) and
 230 consisting of 42 levels in the vertical (model top = 10 hPa) for the 3D fields, over the entirety of
 231 the outermost domain. The changes applied represent a major warming of the region over the
 232 whole troposphere, but specifically over its upper levels. Surface temperature increases on
 233 average by 4.3°C. Alongside the warming, is a decrease in the zonal component of wind and an
 234 increase of the sea level pressure in the central Mediterranean, as detailed in the Supporting
 235 Information Text S1 and Fig S1.

236 2.4 Analyzed Rainfall Parameters and Statistical Methods

237 The parameters examined here are based on the 10-min rainfall fields from the innermost
 238 domain of both the historic and the “future” (PGW) simulations. Rainfall parameters from the
 239 historic and future simulations were compared both through their entire distribution across all
 240 events and through an event-based paired comparison (historic-future). To enable comparison
 241 between events of different magnitudes, in many instances we normalize the quantity examined
 242 to its historic value: $100 \times \frac{\text{future}_i - \text{historic}_i}{\text{historic}_i}$, where i indicates a specific event for which “future”
 243 and “historic” quantities are spatially averaged.

244 The following rainfall parameters were considered for each event:

- 245 (1) Rainfall accumulation for each pixel.
- 246 (2) Areal mean rainfall accumulation, which is the average of (1) over the region of interest.
- 247 (3) Factors affecting areal mean rainfall accumulation: the value in (2) above can be obtained by
 248 integrating rain rates over all rainy pixels and timesteps and divide by the area of the region.
 249 Therefore, it is possible to consider three factors affecting the areal mean accumulation:
 - 250 (a) The mean conditional rain rate is the average of rain rates $>0.1 \text{ mm h}^{-1}$ over all timesteps
 251 and pixels.
 - 252 (b) The duration of the events is defined here as the time it took the central 90% of rainfall
 253 mass to precipitate.

254 (c) The rain area of the event is the time-average of the area covered by 10-min rain rates
 255 $>0.1 \text{ mm h}^{-1}$ along the event. We also examine the rain area for higher rain rate thresholds
 256 in the range of $0.5\text{-}100 \text{ mm h}^{-1}$.

257 (4) Maximal rain rates for durations of 10, 20 and 30 min, 1, 3, 6, 12 and 24 h for each pixel. To
 258 diminish the effect of single outlier pixels, the rain field is first smoothed spatially using a 3X3
 259 pixel moving average window.

260 (5) Regionally maximal rain rates for the same durations as in (4), which are taken as the
 261 maximal value from (4) over all pixels in the region.

262 The analyses above were evaluated both over the entire study region and over four sub-
 263 regions (Fig. 1b). These are the Mediterranean Sea area, the land area, and a division of the latter
 264 to the area north to the 200 mm isohyet roughly corresponding to the Mediterranean climate
 265 zone, and the area south of the 200 mm isohyet roughly corresponding to the desert climate zone.

266 To analyze changes in the spatial structure of precipitation we compared the spatial
 267 autocorrelation structure of the 10-min rain fields whenever these were considered as having
 268 convective elements, following Marra and Morin (2018). Convective elements are defined here
 269 as spatially connected regions of area $\geq 3 \text{ km}^2$ with rain rates $>10 \text{ mm h}^{-1}$ that include at least one
 270 pixel with rain rate $>25 \text{ mm h}^{-1}$. Following Peleg et al. (2013), the spatial autocorrelation was
 271 calculated through fitting a three-parameter exponential function to the 2D spatial
 272 autocorrelation field (e.g., Nerini et al., 2017) of each of the convective rain fields as in Eq. 2:

$$273 \quad r(h) = ae^{-\left(\frac{h}{b}\right)^c}, \quad (2)$$

274 where h is the lag distance, b , termed the correlation distance, is the distance at which the
 275 correlation decreases to $r = ae^{-1}$, a is the nugget (interception) parameter and c is the shape
 276 parameter. For each event, the representative parameters of Eq. (2) are the intra-event medians
 277 over all convective rain fields. The comparison of the autocorrelation structure between historic
 278 and future events is based on the inter-event medians of these representative parameters.

279 Statistical significance of the changes in *pixel*-based parameters is determined through
 280 the paired t-test with 5% significance level. For event-based parameters, statistical significance is
 281 declared if both paired t-test and paired Wilcoxon signed-rank tests are statistically significant at
 282 the 5% level.

283 **3 Results**

284 To have a better understanding of the changes between “future” (PGW) and historic
 285 simulations, we first present an examination of the first HPE in our collection, which exhibits
 286 many of the features observed throughout the events. It is followed by the results obtained
 287 throughout the HPEs collection.

288 **3.1 Case Study #1**

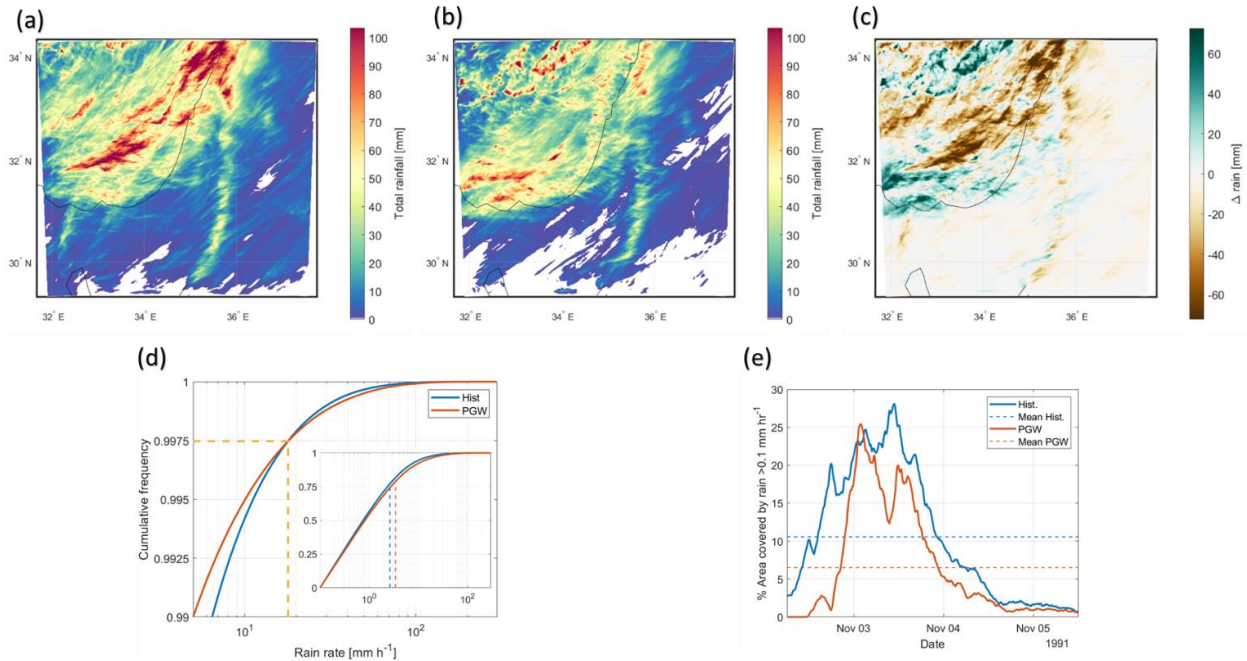
289 The first HPE in our collection (2-5 Nov 1991) is characterized by the passage of a MC,
 290 triggering numerous rain cells crossing the region with a general SW-NE track. These rain cells
 291 contributed $>100 \text{ mm}$ of accumulated rainfall mainly to the north coast and mountainous areas of
 292 the study region (Fig. 2a, Movie S1). The areal average rainfall accumulation simulated over the
 293 entire domain for the historic event is 21.9 mm . Compared to the historic event, the future event

294 exhibits a pronounced (-20%) decrease in precipitation with areal average rainfall accumulation
295 summing to 17.5 mm (Fig. 2b-c). The decrease is more pronounced over the land area (-28%)
296 compared to the sea area (-16%), and is similar between the desert and Mediterranean regions of
297 the land area (-29% and -27%, respectively).

298 In contrast to the decrease in total rain amounts, short duration (10-min) rain rates reveal
299 a more complicated pattern (Fig. 2d). When considering the distribution of all 10-min timesteps
300 and pixels, including those with no-rain (i.e., unconditional rain rates), most of the distribution
301 presents decreased rain rates and only the uppermost quantiles (>99.75%) of future rain rates
302 increase compared to the historic ones. For example, the 99.99% quantile (corresponding to ~ 1.4
303 10^4 pixel-timesteps values of 10-min rain rates), is increased by 21% (from 77 mm h⁻¹ to 93 mm
304 h⁻¹). However, the decrease in most of the unconditional rain rate quantiles is very much affected
305 by the change in the spatiotemporal coverage of the event, namely the wet-frequency.
306 Conversely, considering the distribution of the rainy pixels and timesteps, i.e., the conditional
307 10-min rain rate, quantiles of the future HPE are increasing throughout the distribution (Fig. 2d
308 inset). The mean value of the conditional rain rate increases from 2.64 mm h⁻¹ for the historic
309 event to 3.43 mm h⁻¹ for the future one (+30%).

310 In addition to the mean conditional rain rate, two other factors affect the areal mean
311 rainfall (Sect. 2.4), the duration and the rain area (Fig. 2e). The duration of the event (Fig. S2a)
312 decreased from 2440 min to 1850 min (-24%) between the historic and future simulations. This
313 reduction reflects a delayed start of the “core” of the rainfall during the passage of the MC, and
314 an earlier termination (Movie S1). The rain area (Fig. 2e) exhibits a major contraction (-38%)
315 between the historic and future simulations, from 31.9 10^3 km² (10.5% of the study region) to
316 19.7 10^3 km² (6.5%) in historic and future simulations, respectively. This major decrease in rain
317 area reflects the decrease in the area of precipitating rain cells, seen clearly in Movie S1, as well
318 as in their number. However, it is important to note that we leave for future work a quantitative
319 assessment or tracking of individual rain cells (e.g., Belachsen et al., 2017; Peleg & Morin,
320 2012). Nevertheless, we did compute the spatial autocorrelation of convective rainfall (Sect. 2.4).
321 The spatial autocorrelation distance is 7 km and 5 km, respectively for the historic and future
322 events (Fig. S2b). In addition, the number of 10-min convective timesteps decreases by 5.1%
323 (from 429 to 407).

324 In summary, this case study of the first HPE in our collection indicates that, moving from
325 historic to future climates, areal mean rainfall accumulation decreases whereas conditional 10-
326 min rain rates increase. This opposing behavior is caused by the decrease in the duration of the
327 rainfall and even a greater decrease in the rain area, where the latter is probably due to the
328 reduction in the area of precipitating rain cells and possibly in their number. The decrease in
329 duration and in rain area, which means a decrease in wet-frequency, leads also to a decrease in
330 almost all quantiles (except the uppermost ones) of the unconditional rain rate distribution, while
331 the conditional rain rate distribution presents an increase in all quantiles.



332

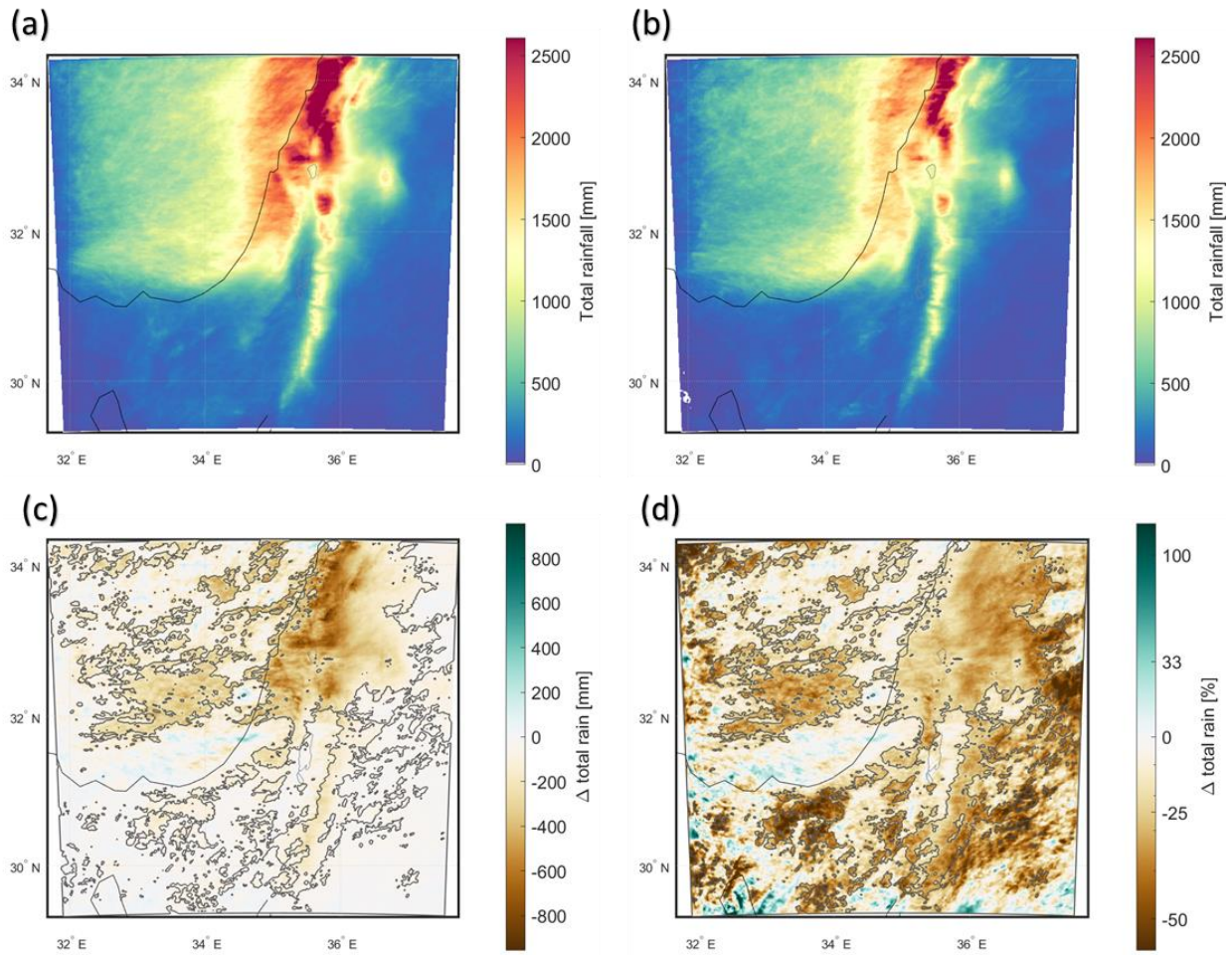
333 **Figure 2.** Rainfall in HPE#1 (2-5 Nov 1991). (a) Total rainfall for the historic simulation (see
 334 Armon et al. (2020): Fig. 7 for a comparison with precipitation measured by the weather radar).
 335 (b) Total rainfall for the future (PGW) simulation. (c) Difference between historic and future
 336 simulations (future – historic). (d) Upper 1% quantile of the cumulative frequency curve of
 337 unconditional 10-min rain rates throughout the event (i.e., including no-rain intervals and pixels)
 338 for the historic (blue line) and future (orange) events. The dashed yellow line marks their
 339 intersection. The small inset presents the full cumulative frequency curve of conditional 10-min
 340 rain rates (where rain rate $>0.1 \text{ mm h}^{-1}$), with mean rain rates in dashed lines. (e) Time series of
 341 the areal coverage of rainfall (% of the area covered by rain rate $>0.1 \text{ mm h}^{-1}$). Note the larger
 342 historic relative to the future unconditional rain rates (up to the 99.75% quantile [marked with
 343 yellow dashed line]; panel d) and the rain area (e) while future conditional rain rates are larger
 344 throughout the distribution (inset in d and Fig. S2a).

345

3.2 Decreased Rainfall Accumulation Throughout Events

346

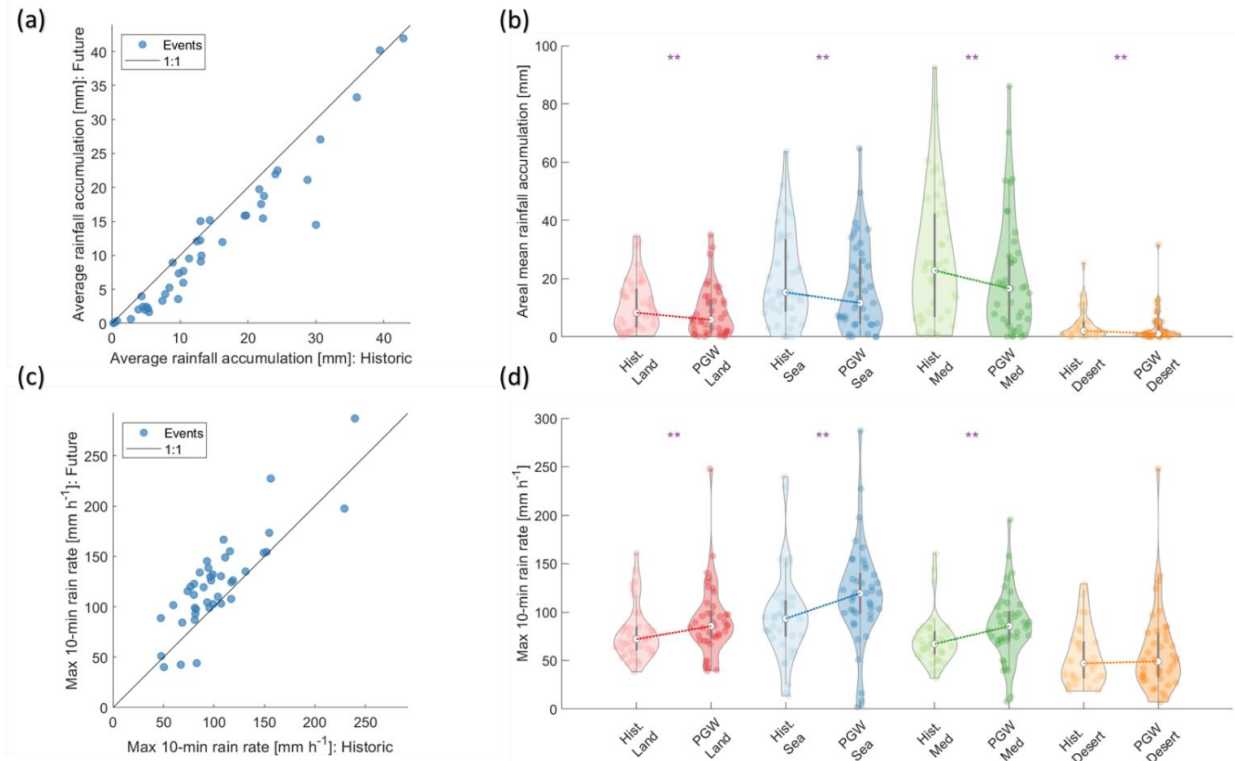
In general, future simulations show a significant decrease in rainfall accumulation
 347 compared with historic simulations (Fig. 3), with a sum of the areal average over all 41 events of
 348 485 mm, compared to 601 mm, respectively (-19%). This decrease is seen throughout the region,
 349 with $>90\%$ of the area exhibiting decreased rainfall. Given the large variability in rainfall in the
 350 region (inter-annual, inter- and intra-event), the fact that 35% of the area shows a significant
 351 change in rainfall accumulation highlights the robustness of the results. Out of the portion of
 352 pixels showing a statistically significant change, 99.97% exhibit a decrease in total rainfall. In
 353 absolute terms, this decrease is most severe in the wetter part of the region (the northern area and
 354 the mountains); 1% of pixels show a decrease of $\geq 618 \text{ mm}$ (Fig. 3c). In relative terms, the
 355 decrease is most drastic over the Sinai desert and throughout Jordan; 1% of pixels show a
 356 decrease of at least 55% (Fig. 3d).



357

358 **Figure 3.** Total rainfall summed over the 41 HPEs historic (a) and future (PGW) simulations. (c)
 359 Difference between historic and future simulations (future – historic). Statistically significant
 360 differences are demarcated by gray lines. (d) Same as (c) but in relative terms: $(100 \times$
 361 $\frac{\text{future} - \text{historic}}{\text{historic}})$.

362 The decrease in rainfall accumulation recognized above for the first HPE is preserved
 363 among most of the analyzed HPEs. More than 90% of events feature smaller rainfall
 364 accumulations in future compared to historic simulations (Fig. 4a, Table 1) with a significant
 365 inter-event average decrease of -2.8 mm (equivalent to -30%). Like the first case study, the
 366 decrease is more pronounced over land compared to the sea with a significant change of -36%
 367 and -26% in average precipitation, respectively. Similarly, 95% and 83% of HPEs were smaller
 368 in future compared to historic simulations over land and sea, respectively. The decreased
 369 precipitation is significant in each of the sub-regions considered here (Fig. 4b, Fig. S3, Table 1).



370

371 **Figure 4.** Comparison of future and historic areal mean rainfall accumulation for all 41 HPEs
 372 analyzed (a-b, Sect. 3.2), and the regional maximal 10-min rain rates (i.e., along all the pixels in
 373 the region and throughout timesteps) (c-d, Sect. 3.4). Scatter plots (a, c) compare the historic
 374 (horizontal axis) and future (vertical axis) values. Violin plots (b, d) show the distribution of
 375 historic (pale colors) and future (bold colors) quantities for the different sub-regions (Fig. 1b).
 376 Each dot along the violin represents a value of one HPE, white dots are median values, and gray
 377 boxes are the inter quartile range. The change between medians of historic and future events is
 378 marked with dashed lines. Statistically significant differences between the paired-event
 379 populations for each region (presented also as scatter plots in Fig. S3 and S7) are marked here
 380 with ** (see also Table 1).

381

382 **Table 1:** Changes in rainfall properties between future and historic simulations. Bolded numbers
 383 are statistically significant (i.e. on both paired t- and paired Wilcoxon signed-rank tests, Sect.
 384 2.4). Italics are significant on the paired t-test only. The upper value represents the entire region
 385 and below are values for each sub-region (land, sea, med=Mediterranean, and des=desert, Fig.
 386 1b).

| | Fraction of HPEs exhibiting larger values in future [%] | | | | Average normalized change: $\frac{1}{n} \sum_{i=1}^n \left(\frac{future_i - historic_i}{historic_i} \right)$ [%] | | | |
|--|--|-----|-----|-----|---|------------|------------|------------|
| Areal average rainfall accumulation | 10 | | | | -30 | | | |
| | Land | Sea | Med | Des | Land | Sea | Med | Des |
| | 5 | 17 | 10 | 12 | -36 | -26 | -34 | -37 |
| Regionally max 10-min rain rate | 85 | | | | 22 | | | |
| | Land | Sea | Med | Des | Land | Sea | Med | Des |
| | 80 | 83 | 83 | 63 | 18 | 23 | 21 | 11 |
| Duration | 24 | | | | -9 | | | |
| | Land | Sea | Med | Des | Land | Sea | Med | Des |
| | 24 | 29 | 24 | 37 | -8 | -7 | -8 | 2 |
| Rain area | 2 | | | | -40 | | | |
| | 2 | 2 | 2 | 2 | -42 | -38 | -41 | -42 |

387

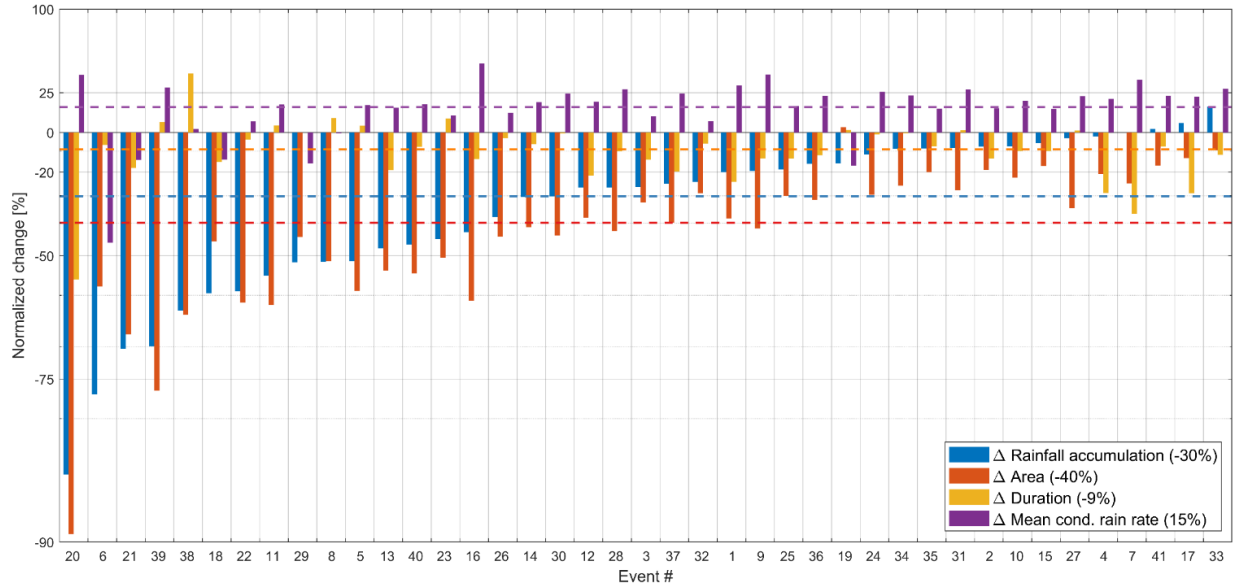
388 3.3 Opposing Changes in Rainfall Properties: Increased Conditional Rain Rates, 389 Decreased Duration and Areal Coverage

390 Changes in the event-based areal mean rainfall accumulation are examined through
 391 changes in three rainfall components: mean conditional rain rate, event duration, and rain area
 392 (Fig. 5, Fig. S4-S5). The mean conditional rain rate significantly increases with an average
 393 change of 15%, and >85% of the events show higher average conditional rain rate in the future
 394 compared with the historic simulations. Although there is some correlation between the changes
 395 in mean conditional rain rate and total rainfall (Spearman's correlation: $\rho = 0.37$; Fig. S5)
 396 increases as large as 47% (event #16) are observed in events with a reduction of the rainfall
 397 accumulation. This suggests that the change in the mean conditional rain is rather weakly related
 398 to rainfall accumulation.

399 While mean conditional rain rate is increasing, the duration of events shows a significant
 400 negative change (-9%), from a mean of 3290 min to 2980 min, and >75% of the events are
 401 longer in historic compared to future simulations (Table 1). The reduction in durations is not,
 402 however, a good predictor for the reduction in total rainfall accumulation, with a low, non-
 403 significant negative correlation between the two (Fig. S5).

404 The third component in this analysis, the rain area, reveals the largest relative change out
 405 of all three components. It also presents the highest correlation with the change in rainfall
 406 accumulation ($\rho = 0.93$; Fig. S5). The rain area is decreased in all but one of the events (>97%
 407 of events) with a significant and substantial average decrease (-40%). Events with the lowest

408 reduction (or even slight increase) in rainfall accumulation are only those in which the reduction
 409 in the rain area is relatively small, while events with a large decrease in rainfall accumulation are
 410 accompanied by a large decrease in rain area. These results indicate that the factor most heavily
 411 related to changes in rainfall accumulation is the rain area.



412

413 **Figure 5.** Normalized change between future and historic simulations ($100 \times \frac{\text{future-historic}}{\text{historic}}$) for
 414 the 41 HPEs analyzed. Events are sorted by the change in rainfall accumulation (blue bars).
 415 Dashed lines represent average inter-event values (written also inside the legend). The non-
 416 normalized changes are shown in Fig. S4. Correlations between the change in rainfall
 417 accumulation and the three other parameters are in Fig. S5.

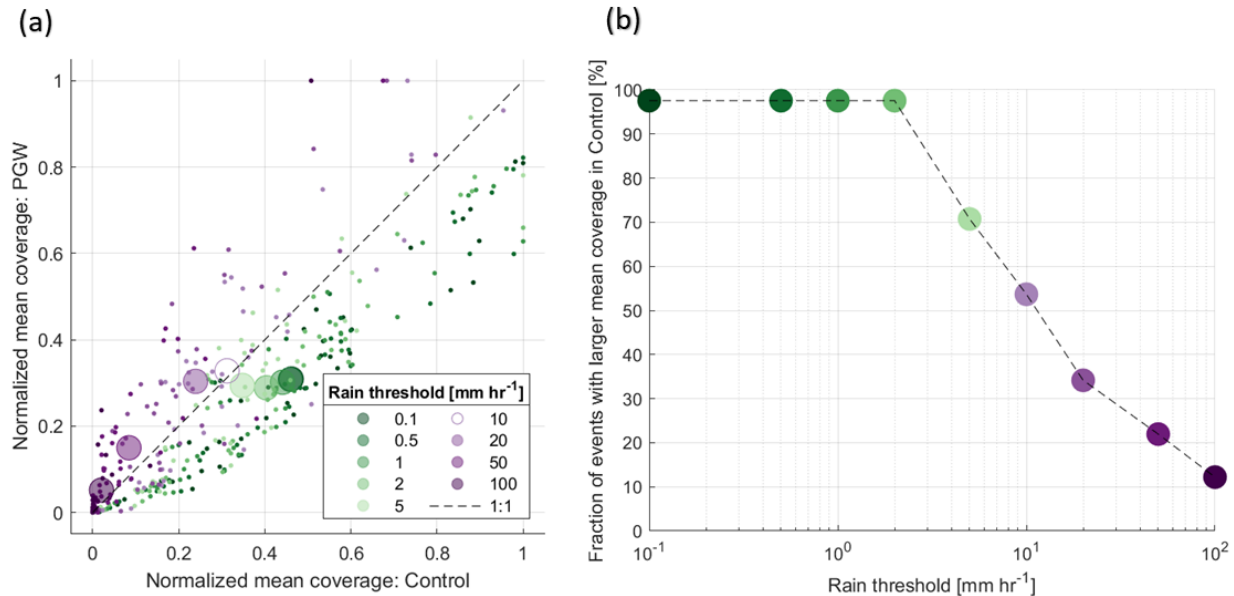
418

3.3.1 Spatial Concentration of Future Rainstorms

419 To better understand the changes in the rain area, we examine its changes using a range
 420 of rain rate thresholds. Divergent changes in the extent of areas exceeding various rain rates are
 421 essential in understanding possible hydrological responses to climate change (Bacchi & Ranzi,
 422 1996; Fowler, Lenderink, et al., 2021; Peleg et al., 2018). Fig. 6a displays the event-average
 423 areal rainfall coverage for each HPE with different rain rate thresholds, normalized by the largest
 424 coverage for each intensity for both historic and future simulations. The fraction of events with
 425 larger areal coverage for each rain rate threshold in historic events, i.e., the relative number of
 426 points below the 1:1 line, is displayed in Fig. 6b. The areal coverage of rainfall with relatively
 427 low rain rates ($0.1-5 \text{ mm h}^{-1}$) is reduced significantly for future compared to historic simulations.
 428 The opposite case is true for high rain rates ($20-100 \text{ mm h}^{-1}$). This change occurs at rain rates of
 429 $\sim 10 \text{ mm h}^{-1}$, where no significant change is documented between rain area above this threshold
 430 in historic and in future simulations.

431 These different trends imply that when compared with historic rainstorms, the total “wet”
 432 area in future events is lower, and the storms are more concentrated around the higher rain rates.
 433 This conclusion is further strengthened by the change in the autocorrelation pattern of convective
 434 rainfall, which demonstrate a much sharper decrease with distance in future compared with

435 historic simulations and, accordingly, the median of the autocorrelation distance decreases from
 436 8 km to 5 km (Fig. S6).

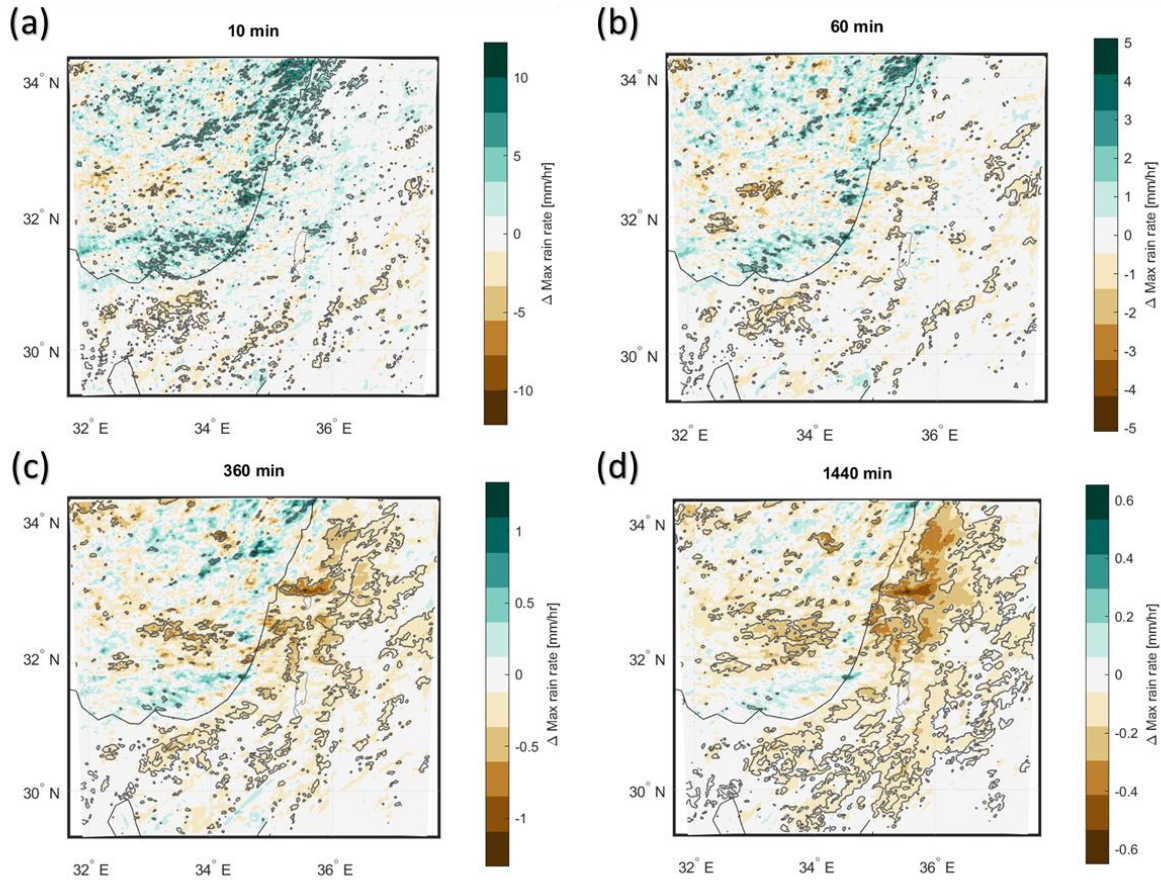


437

438 **Figure 6.** Changes in areal coverage for different rain rate thresholds. (a) Areal mean coverage
 439 along each event (small dots) for different rain intensity thresholds (different colors) in historic
 440 events (horizontal axis) and future (PGW) events (vertical axis). Values are normalized by the
 441 maximal value observed for each rain rate threshold. Average inter-event values are marked with
 442 large circles. Filled circles demonstrate statistically significant changes between future and
 443 historic values, and one hollow circle shows an insignificant difference. (b) Fraction of events
 444 with larger areal coverage in historic compared to future simulations for each of the inspected
 445 rain rate thresholds.

446 3.4 Changes in Extreme Rain Rates for Different Durations

447 The change in maximal rain rate for each pixel displays different behavior along the
 448 study area and between durations. The maps in Fig. 7 show the difference between the inter-
 449 event average of the maximum rain rate per event for each pixel, over durations of 10-min to 24-
 450 h. For short durations (10-60 min, Fig. 7a-b, Fig. S7), a north-south gradient in maximal rain
 451 rates is evident in maximal rain rates. Significant decreases are identified mainly over the
 452 southern and eastern desert areas and far into the sea. In contrast, a positive change sub-parallel
 453 to the coastline and over Lebanon is present. It is observed mainly a few kilometers offshore and
 454 over the mountains at the north of the study region. Over longer durations (a few hours to one
 455 day), a larger portion of the region exhibits a significant change in maximal rain intensities (Fig.
 456 7c-d, Fig. S7). This change is almost exclusively negative, focusing over both the desert area and
 457 most of the northern land region (excluding the shoreline and the upslopes of the Lebanon
 458 Mountains). In relative terms, for the longer durations, almost 25% of the area exhibits a
 459 decrease of more than 40% compared with areal-average maximal rain rate in historic events
 460 (Fig. S7). It must be noted, however, that the spatial perspective presented in Fig. 7 involves both
 461 the increase in rain rates, and the decrease in wet-frequency caused by smaller areal coverage of
 462 these intensities and shorter event durations, resulting in a mixture of increased and decreased
 463 maximal rain rates.



464

465 **Figure 7.** Changes in maximal rain rates averaged over all events for durations of 10-min (a), 1 h
 466 (b), 6 h (c) and 24-h (d) between future and historic simulations (future – historic). Statistically
 467 significant differences are circumscribed in gray.

468 In contrast to the decrease in rainfall accumulation, and as exemplified by the first case
 469 study (Sect. 3.1), regionally maximal 10-min rain rates (maximum along all pixels and timesteps)
 470 in future simulations are significantly higher than in historic simulations (Fig. 4c-d, Table 1) with
 471 an average increase of 22%. This conclusion holds for all sub-regions inspected here, except for
 472 the desert sub-region, in which the increase (11%) is non-significant (Fig. 4d, Fig. S8, Table 1).
 473 Increases of the regionally maximal 10-min rain rates over both the Mediterranean climate and
 474 Sea sub-regions are on average $>21\%$, and the increase over land, as a result of the small
 475 increase over the desert, is 18%. Furthermore, most of the events (85%) have higher values in
 476 future compared to historic simulations and this is rather consistent among the different sub-
 477 regions (Table 1). The increase in regionally maximal rain rates between historic and future
 478 simulations holds for longer durations as well (Fig. S9).

479

480

481 **4 Summary and Discussion**

482 This study shows the changes in rainfall patterns between paired simulations of historic
483 and future HPEs, with the objective of identifying whether common changes in rainfall patterns
484 exist, and characterizing these changes. The collection of objectively identified 41 HPEs was
485 simulated twice, and the results of the two simulations are compared. The first simulation is
486 based on historic conditions, and the second applies expected changes in various meteorological
487 parameters from the RCP 8.5 scenario for the end of the 21st century on top of historic initial and
488 boundary conditions. Selected events represent some of the heaviest precipitation events in the
489 region around the end of the 20th century. Our results, shown first for a case study, and then for
490 the full collection of HPEs, demonstrate the added value of using event-based simulations, and
491 provide high resolution projections of future changes in rainfall patterns, highlighting the
492 importance of changes in specific rainfall constituents, as discussed below.

493 4.1 Opportunities Gained by the Event-Based Approach and their Implications

494 Large-scale and long term CPM simulations are becoming increasingly attainable,
495 allowing to better characterize precipitation extremes in future climate scenarios (e.g., Coppola
496 et al., 2020; Kendon et al., 2018). However, there are still difficulties in providing reliable
497 projections of rainfall during HPEs (Kendon et al., 2021); the computational and the power
498 consumption costs of these simulations are huge (Fuhrer et al., 2018; Loft, 2020), and the rarest
499 of extremes are difficult to characterize even in runs extending for many years. Therefore, if the
500 purpose of a study is to identify potential changes in only a subset of the climate, e.g., HPEs, a
501 full-climate run should be used prudently.

502 Here, using an event-based approach we were able to show plausible impacts of climate
503 change on some of the heaviest rainstorms in the eastern Mediterranean. Furthermore, we show
504 that many “plausible” instances (i.e., individual HPE events) point in the same direction;
505 therefore, the plausible scenario may be considered as the probable scenario. Even if the entire
506 variance of possibilities is not perfectly represented using this method, the emerging similar
507 response enables us to garner insight on “*climate* questions”, such as projections of future
508 precipitation patterns, using a *weather* model. We showed that rainfall accumulation under
509 global warming conditions decreases over > 90% of the simulated HPEs and analyzed the
510 properties of rainfall accounting for this decrease. The rain area exhibits the largest and most
511 consistent decrease and is heavily associated with the decrease in rainfall accumulation, while
512 increased conditional rain rate is only weakly related to rainfall accumulation and cannot
513 counteract the decreased rain area.

514 The simulated change in rainfall patterns can have considerable implications both on
515 water resources and on natural hazards, which can be illuminated if we focus on specific
516 rainstorms. For example, event #8 (1-7 Nov 1994) is an infamous ARST storm in which more
517 than 500 people lost their lives, and extensive floods and damages occurred in Egypt and Israel
518 (Krichak et al., 2000; De Vries et al., 2013). This event shows a substantial reduction in total
519 rainfall under future-simulated conditions (-51%; Fig. 5, Fig. S10). Such a reduction would
520 probably lead to a reduced risk of flash flooding, especially at the northern part of the region.
521 However, while in many places total rainfall decreased in the simulation, few high-intensity rain
522 cells still impacted the Sinai desert (Movie S2), with total rainfall of >100 mm, which would
523 undoubtedly cause substantive floods in this region.

524 HPE #12 (Fig. S11) triggered a major streamflow increase and raised the level of the Sea
525 of Galilee, the largest surficial freshwater reservoir in the region, by 45 cm within a week
526 (compared with <10 cm rise the week before the storm occurred). This rise is equivalent to the
527 yearly industrial consumption of freshwater in Israel at that time ($\sim 90 \times 10^6 \text{ m}^3$) and constitutes
528 more than a fifth of the annual water rise of the lake. The simulation of the future event indicates
529 a substantial decrease in total rainfall (-27%). As the hydrological response to decreases in
530 rainfall is non-linear (e.g., Peleg et al., 2014), this would probably lead to an even larger decrease
531 in freshwater recharge with major implications on water resources. While a hydrological
532 simulation of the different events is out of the scope of this paper, we stress that to have better
533 insights about the hydrological response, a comparison of historic and future simulations of
534 specific events through a hydrological model is highly desired.

535 It is important to note that the frequency of events (e.g., Myhre et al., 2019) is not
536 implicitly considered in our simulations. Rain events in the region are projected to have a
537 reduced frequency ($\sim 20\%$; Hochman et al., 2018; Zappa et al., 2015), and thus, the decreased
538 rainfall we show here for the specific simulated events, may be considered as an underestimation
539 of the projected changes in total precipitation from HPEs accounting for event occurrences.

540 Nevertheless, a minor shortcoming of the PGW methodology is that frequency data is not
541 totally excluded from the applied changes, which arise from the climatology of 25 years of
542 CMIP5 models' simulations. For this reason, changes in specific properties of events should be
543 reflected by the mean climatology. Meaning that if our simulations would constitute a large
544 portion of a 25-yr time interval, they would affect the mean climatology as well. Forty-one
545 HPEs, however, are not a substantial part of the climatological mean of 25 years ($\sim 3\%$ of the
546 days in the season we examine [Oct-Apr]), and thus our simulations are not expected to be
547 severely biased by this issue.

548 A potential limitation that this study can be criticized for is the use of a single climate
549 scenario forcing for the PGW and as such it will give only plausible results, rather probable.
550 However, (a) this single scenario is the ensemble mean of CMIP5 models, which can be
551 considered as a best estimate, to date, of large scale future changes, though work currently in
552 progress shows that CMIP6 models generally simulate similar, and if anything more severe,
553 changes to CMIP5 in this region (not shown), (b) we use a collection of many objectively-
554 identified events that constitutes some of the highest magnitude HPEs in the region. Results for
555 this large set of paired-simulations show a similar behavior of different events representing
556 different synoptic-scale conditions. Therefore, we claim that the sign and magnitude of the
557 changes that emerge from these simulations should be considered as a probable projection of
558 HPEs in the region.

559 Indeed, the PGW event-based methodology provides us with projections for HPEs in a
560 warmer climate. However, it must be noted we do not attempt to provide a climatology of HPEs
561 in the future, nor give updated extreme event levels and frequencies. While these can be obtained
562 using a framework which accounts for the frequency of events (Marra et al., 2019), the results
563 we obtain have significance in drawing possible future scenarios for some of the heaviest
564 precipitation events in the region. High resolution rainfall projections can also help improving
565 future predictions in approaches requiring a changed rainfall distribution (e.g., Marra et al.,
566 2021).

567 4.2 Changes in Rainfall Patterns During Rainstorms

568 Future rainstorms simulated in this work show quite a difference in rainfall patterns
569 compared to historic rainstorms, mainly being more concentrated in both space and time. Given
570 that the conditional rain rate increases, one might expect an increase in total precipitation during
571 heavy precipitation events, as projected, for example, over Europe (e.g., Y. Chen et al., 2020;
572 Hawcroft et al., 2018; Kendon et al., 2014). However, two other factors, less often addressed,
573 negatively affect total rainfall: the size of the rain area, and the duration of the events. Among
574 these two, we find that the rain area is the main contributor to decreased rainfall accumulation,
575 which decreases, on average, by 40%. Furthermore, the rain area has a high correlation with the
576 changes in rainfall accumulation, while the event duration decreases on average by 9% and has a
577 low correlation with rainfall accumulation changes.

578 It must be noted, however, that the changes in the rain area are not constant over different
579 rain rates thresholds. The baseline 0.1 mm h^{-1} intensity is a good proxy for the total storm area.
580 Going to larger thresholds, the area represented is a better indicator for the intense “core” of the
581 storm, namely the inner part of convective cells during the storm. In fact, we found an increase in
582 the rain area for thresholds of $>10 \text{ mm hr}^{-1}$. This means that, although the total rain area of HPEs
583 shrinks, their cores are getting larger in future simulations. Similar findings were reported by
584 Peleg et al. (2018) using historic radar observations over the eastern Mediterranean and by
585 Wasko et al. (2016) using rain gauges in Australia. Both studies showed that total rain area and
586 the convective core area scale with temperature in opposite directions: total area exhibits a
587 negative scaling, while the area of the convective cores is positively scaled with temperature; this
588 is probably related to an enhanced moisture convergence into the convective cores from the total
589 storm extent. In contrast, results from studies of future extreme precipitation in the Netherlands
590 and in the UK show the area of the storms is expected to increase with global warming (Y. Chen
591 et al., 2020; Lochbihler et al., 2017, 2019), which may indicate a regional dependence in the
592 scaling of the rain area, but this topic should be addressed in future studies (Fowler, Lenderink,
593 et al., 2021).

594 Since the hydrological response to HPEs is heavily related to space-time precipitation
595 characteristics, the results shown above would have an immense impact on the hydrology of
596 future rainstorms. Larger storm cores, having increased short duration rain rates may increase the
597 risk of urban flooding and short-lived, fast responding flash floods (e.g., Tarasova et al., 2019),
598 as well as soil erosion (e.g., Shmilovitz et al., 2021). However, this effect is expected to be
599 mitigated by the decreased rainfall frequency caused by the shorter storm duration and smaller
600 overall area. Combined, a possible conclusion could be that over the affected (rainy) area, the
601 risk of short-duration natural hazards is higher, while over the entire domain this is uncertain.
602 Yet, a clearer conclusion can be drawn for the detrimental effects of the changes in rainfall
603 patterns over the entire storm through longer-duration processes: mean rain rates and amounts
604 are expected to dramatically decrease. Therefore, the expected hydrological impact would
605 include a further reduction of streamflow and a decline in freshwater resources, which requires
606 immediate address by policy makers.

607 Two key aspects are missing from the results presented here: a detailed analysis of the
608 meteorological factors affecting the modeled change in rainfall patterns and their scaling with
609 temperature, and a modeling of the hydrological impact of these changes. These two prospective
610 aspects are currently being further studied. We call for a continued use of the PGW methodology

611 as a relatively easy-to-implement experiment, with results relevant to events of specific interest
612 such as HPEs.

613 **5 Conclusions**

614 Through high-resolution event-based simulations of eastern Mediterranean HPEs in
615 present and future climate, we show that in future: (a) event rainfall accumulations decrease
616 substantially (inter-event average = -30%), throughout the study region, (b) mean conditional
617 rain rate is increased (+15%), (c) event duration is getting shorter (-9%), and (d) rain area
618 becomes dramatically smaller (-40%). The areal coverage for various rain rates shows opposing
619 changes for lower and higher rain rates: it is reduced for low rain rate thresholds, and expanded
620 for high rate thresholds. Thus, rainstorms become more concentrated in future simulations, with
621 convective cores that exhibit shorter autocorrelation distance and higher regionally maximal rain
622 rates (+22%). Furthermore, some increases in local short duration rain rates are seen mostly over
623 the coastal region, but long duration rain rates are decreased throughout the region. The changes
624 found are rather consistent across events, suggesting that these event-based conclusions may
625 actually be probable. Changes in rainfall properties identified here reveal the dominance of the
626 rain area in determining the decrease in total rainfall, with great implications over future
627 hydrological processes.

628 **Acknowledgments, Samples, and Data**

629 The authors thank Y. Shmilovitz and R. Dann for both fruitful discussions and help with
630 coding issues. This research has been supported by the Israel Ministry of Science and
631 Technology (grant no. 61792) and the Israel Water Authority. Shacham radar data for the 41
632 HPEs are available online (<https://doi.org/10.5281/zenodo.5353714>). ERA-Interim data were
633 downloaded from the Research Data Archive at the National Center for Atmospheric Research,
634 Computational and Information Systems Laboratory (<https://doi.org/10.5065/D6CR5RD9>).
635 CMIP5 data were downloaded from the ESGF Node at DKRZ ([https://esgf-
637 data.dkrz.de/projects/esgf-dkrz/tou](https://esgf-
636 data.dkrz.de/projects/esgf-dkrz/tou)). The WRF namelist.input file can be found in the Supporting
638 Information. FM was supported by the Institute of Atmospheric Sciences and Climate (ISAC) of
639 the National Research Council of Italy (CNR).

640 **References**

- 641 Alpert, P., & Shay-EL, Y. (1994). The moisture Source for the Winter Cyclones in the Eastern
642 Mediterranean. *Israel Meteorological Research Papers*, 5, 20–27.
- 643 Alpert, P., Ben-Gai, T., Baharad, A., Benjamini, Y., Yekutieli, D., Colacino, M., et al. (2002).
644 The paradoxical increase of Mediterranean extreme daily rainfall in spite of decrease in
645 total values. *Geophysical Research Letters*, 29(11), 1536.
646 <https://doi.org/10.1029/2001GL013554>
- 647 Armon, M., Dente, E., Smith, J. A., Enzel, Y., & Morin, E. (2018). Synoptic-scale control over
648 modern rainfall and flood patterns in the Levant drylands with implications for past
649 climates. *Journal of Hydrometeorology*, 19(6), 1077–1096. [https://doi.org/10.1175/JHM-D-
18-0013.1](https://doi.org/10.1175/JHM-D-
650 18-0013.1)
- 651 Armon, M., Morin, E., & Enzel, Y. (2019). Overview of modern atmospheric patterns

- 652 controlling rainfall and floods into the Dead Sea: Implications for the lake's sedimentology
653 and paleohydrology. *Quaternary Science Reviews*, 216, 58–73.
654 <https://doi.org/10.1016/j.quascirev.2019.06.005>
- 655 Armon, M., Marra, F., Enzel, Y., Rostkier-Edelstein, D., & Morin, E. (2020). Radar-based
656 characterisation of heavy precipitation in the eastern Mediterranean and its representation in
657 a convection-permitting model. *Hydrology and Earth System Sciences*, 24(3), 1227–1249.
658 <https://doi.org/10.5194/hess-24-1227-2020>
- 659 Ashbel, D. (1938). Great floods in Sinai Peninsula, Palestine, Syria and the Syrian Desert, and
660 the influence of the Red Sea on their formation. *Quarterly Journal of the Royal*
661 *Meteorological Society*, 64(277), 635–639.
- 662 Bacchi, B., & Ranzi, R. (1996). On the derivation of the areal reduction factor of storms.
663 *Atmospheric Research*, 42(1–4), 123–135. [https://doi.org/10.1016/0169-8095\(95\)00058-5](https://doi.org/10.1016/0169-8095(95)00058-5)
- 664 Ban, N., Schmidli, J., & Schär, C. (2014). Evaluation of the convection-resolving regional
665 climate modeling approach in decade-long simulations. *Journal of Geophysical Research*,
666 119(13), 7889–7907. <https://doi.org/10.1002/2014JD021478>
- 667 Belachsen, I., Marra, F., Peleg, N., & Morin, E. (2017). Convective rainfall in dry climate:
668 relations with synoptic systems and flash-flood generation in the Dead Sea region.
669 *Geophysical Research Abstracts EGU General Assembly*. [https://doi.org/10.5194/hess-](https://doi.org/10.5194/hess-2017-235)
670 [2017-235](https://doi.org/10.5194/hess-2017-235)
- 671 Borga, M., Stoffel, M., Marchi, L., Marra, F., & Jakob, M. (2014). Hydrogeomorphic response to
672 extreme rainfall in headwater systems: Flash floods and debris flows. *Journal of Hydrology*,
673 518(PB), 194–205. <https://doi.org/10.1016/j.jhydrol.2014.05.022>
- 674 Brogli, R., Kröner, N., Sørland, S. L., Lüthi, D., & Schär, C. (2019). The role of hadley
675 circulation and lapse-rate changes for the future European summer climate. *Journal of*
676 *Climate*, 32(2), 385–404. <https://doi.org/10.1175/JCLI-D-18-0431.1>
- 677 Cannon, A. J., & Innocenti, S. (2019). Projected intensification of sub-daily and daily rainfall
678 extremes in convection-permitting climate model simulations over North America:
679 Implications for future intensity-duration-frequency curves. *Natural Hazards and Earth*
680 *System Sciences*, 19(2), 421–440. <https://doi.org/10.5194/nhess-19-421-2019>
- 681 Chan, S. C., Kendon, E. J., Giorgia, B., Elizabeth, F., & Fowler, H. J. (2020). Europe-wide
682 precipitation projections at convection permitting scale with the Unified Model. *Climate*
683 *Dynamics*, (submitted(0123456789), 1–23. <https://doi.org/10.1007/s00382-020-05192-8>
- 684 Chen, G., Wang, W.-C., Cheng, C.-T., & Hsu, H.-H. (2020). Extreme snow events along the
685 coast of the northeast United States: Potential changes due to global warming. *Journal of*
686 *Climate*, 1–46. <https://doi.org/10.1175/jcli-d-20-0197.1>
- 687 Chen, J., Wang, Z., Tam, C. Y., Lau, N. C., Lau, D. S. D., & Mok, H. Y. (2020). Impacts of
688 climate change on tropical cyclones and induced storm surges in the Pearl River Delta
689 region using pseudo-global-warming method. *Scientific Reports*, 10(1), 1–10.
690 <https://doi.org/10.1038/s41598-020-58824-8>
- 691 Chen, Y., Paschalis, A., Kendon, E., Kim, D., & Onof, C. (2020). Changing Spatial Structure of
692 Summer Heavy Rainfall, Using Convection-Permitting Ensemble. *Geophysical Research*

- 693 *Letters*, 1–12. <https://doi.org/10.1029/2020gl090903>
- 694 Coppola, E., Sobolowski, S., Pichelli, E., Raffaele, F., Ahrens, B., Anders, I., et al. (2020). A
695 *first-of-its-kind multi-model convection permitting ensemble for investigating convective*
696 *phenomena over Europe and the Mediterranean. Climate Dynamics* (Vol. 55).
697 <https://doi.org/10.1007/s00382-018-4521-8>
- 698 Crook, J., Klein, C., Folwell, S., Taylor, C. M., Parker, D. J., Stratton, R., & Stein, T. (2019).
699 Assessment of the Representation of West African Storm Lifecycles in Convection-
700 Permitting Simulations. *Earth and Space Science*, 6(5), 818–835.
701 <https://doi.org/10.1029/2018EA000491>
- 702 Dayan, U., & Abramski, R. (1983). Heavy rain in the Middle East related to unusual jet stream
703 properties. *Bulletin of the American Meteorological Society*, 64(10), 1138–1140.
- 704 Dayan, U., & Morin, E. (2006). Flash flood – producing rainstorms over the Dead Sea: A review.
705 *New Frontiers in Dead Sea Paleoenvironmental Research: Geological Society of America*
706 *Special Paper*, 401(04), 53–62. [https://doi.org/10.1130/2006.2401\(04\)](https://doi.org/10.1130/2006.2401(04)).
- 707 Dayan, U., Lensky, I. M., Ziv, B., & Khain, P. (2021). Atmospheric conditions leading to an
708 exceptional fatal flash flood in the Negev Desert, Israel. *Natural Hazards and Earth System*
709 *Sciences*, 21(5), 1583–1597. <https://doi.org/10.5194/nhess-21-1583-2021>
- 710 Dee, D. P., Uppala, S. M., Simmons, A. J., Berrisford, P., Poli, P., Kobayashi, S., et al. (2011).
711 The ERA-Interim reanalysis: configuration and performance of the data assimilation
712 system. *Quarterly Journal of the Royal Meteorological Society*, 137(656), 553–597.
713 <https://doi.org/10.1002/qj.828>
- 714 Dirmeyer, P. A., Brubaker, K. L., & DelSole, T. (2009). Import and export of atmospheric water
715 vapor between nations. *Journal of Hydrology*, 365(1–2), 11–22.
716 <https://doi.org/10.1016/j.jhydrol.2008.11.016>
- 717 Donat, M. G., Lowry, A. L., Alexander, L. V., O’Gorman, P. A., & Maher, N. (2016). More
718 extreme precipitation in the world’s dry and wet regions. *Nature Climate Change*, 6(5),
719 508–513. <https://doi.org/10.1038/nclimate2941>
- 720 El-Fandy, M. G. (1946). Barometric lows of cyprus. *Quarterly Journal of the Royal*
721 *Meteorological Society*, 72(314), 291–306. <https://doi.org/10.1002/qj.49707231406>
- 722 Enzel, Y., Bookman (Ken Tor), R., Sharon, D., Gvirtzman, H., Dayan, U., Ziv, B., & Stein, M.
723 (2003). Late Holocene climates of the Near East deduced from Dead Sea level variations
724 and modern regional winter rainfall. *Quaternary Research*, 60(3), 263–273.
725 <https://doi.org/10.1016/j.yqres.2003.07.011>
- 726 Fatichi, S., Ivanov, V. Y., Paschalis, A., Peleg, N., Molnar, P., Rimkus, S., et al. (2016).
727 Uncertainty partition challenges the predictability of vital details of climate change. *Earth’s*
728 *Future*, 4(5), 240–251. <https://doi.org/10.1002/2015EF000336>
- 729 Ferreira, R. N. (2021). Cut-Off Lows and Extreme Precipitation in Eastern Spain : Current and
730 Future Climate.
- 731 Flaounas, E., Röthlisberger, M., Boettcher, M., Sprenger, M., & Wernli, H. (2021). Extreme wet
732 seasons – their definition and relationship with synoptic-scale weather systems. *Weather*
733 *and Climate Dynamics*, 2(1), 71–88. <https://doi.org/10.5194/wcd-2-71-2021>

- 734 Fosser, G., Khodayar, S., & Berg, P. (2014). Benefit of convection permitting climate model
735 simulations in the representation of convective precipitation. *Climate Dynamics*, *44*(1–2),
736 45–60. <https://doi.org/10.1007/s00382-014-2242-1>
- 737 Fowler, H. J., Lenderink, G., Prein, A. F., Westra, S., Allan, R. P., Ban, N., et al. (2021).
738 Anthropogenic intensification of short-duration rainfall extremes. *Nature Reviews Earth &*
739 *Environment*, *2*(2), 107–122. <https://doi.org/10.1038/s43017-020-00128-6>
- 740 Fowler, H. J., Wasko, C., & Prein, A. F. (2021). Intensification of short-duration rainfall
741 extremes and implications for flood risk: Current state of the art and future directions.
742 *Philosophical Transactions of the Royal Society A: Mathematical, Physical and*
743 *Engineering Sciences*, *379*(2195). <https://doi.org/10.1098/rsta.2019.0541>
- 744 Fowler, H. J., Ali, H., Allan, R. P., Ban, N., Barbero, R., Berg, P., et al. (2021). Towards
745 advancing scientific knowledge of climate change impacts on short-duration rainfall
746 extremes. *Philosophical Transactions of the Royal Society A: Mathematical, Physical and*
747 *Engineering Sciences*, *379*(2195). <https://doi.org/10.1098/rsta.2019.0542>
- 748 Fuhrer, O., Chadha, T., Hoefler, T., Kwasniewski, G., Lapillonne, X., Leutwyler, D., et al.
749 (2018). Near-global climate simulation at 1km resolution: Establishing a performance
750 baseline on 4888 GPUs with COSMO 5.0. *Geoscientific Model Development*, *11*(4), 1665–
751 1681. <https://doi.org/10.5194/gmd-11-1665-2018>
- 752 Garfinkel, C. I., Adam, O., Morin, E., Enzel, Y., Elbaum, E., Bartov, M., et al. (2020). The Role
753 of Zonally Averaged Climate Change in Contributing to Intermodel Spread in CMIP5
754 Predicted Local Precipitation Changes. *Journal of Climate*, *33*(3), 1141–1154.
755 <https://doi.org/10.1175/JCLI-D-19-0232.1>
- 756 Giorgi, F., & Lionello, P. (2008). Climate change projections for the Mediterranean region.
757 *Global and Planetary Change*, *63*(2–3), 90–104.
758 <https://doi.org/10.1016/j.gloplacha.2007.09.005>
- 759 Goldreich, Y. (1994). The spatial distribution of annual rainfall in Israel - a review. *Theoretical*
760 *and Applied Climatology*, *50*(1–2), 45–59. <https://doi.org/10.1007/BF00864902>
- 761 Goldreich, Yair. (1995). Temporal variations of rainfall in Israel. *Climate Research*, *5*(2), 167–
762 179. <https://doi.org/10.3354/cr005167>
- 763 Goldreich, Yair. (2012). *The climate of Israel: observation, research and application*. Springer
764 Science & Business Media. <https://doi.org/10.1007/978-1-4615-0697-3>
- 765 Gómez-Navarro, J. J., Raible, C. C., García-Valero, J. A., Messmer, M., Montávez, J. P., &
766 Martius, O. (2019). Event selection for dynamical downscaling: a neural network approach
767 for physically-constrained precipitation events. *Climate Dynamics*.
768 <https://doi.org/10.1007/s00382-019-04818-w>
- 769 Gutmann, E. D., Rasmussen, R. M., Liu, C., Ikeda, K., Bruyere, C. L., Done, J. M., et al. (2018).
770 Changes in hurricanes from a 13-Yr convection-permitting pseudo- global warming
771 simulation. *Journal of Climate*, *31*(9), 3643–3657. <https://doi.org/10.1175/JCLI-D-17-0391.1>
- 773 Hawcroft, M., Walsh, E., Hodges, K., & Zappa, G. (2018). Significantly increased extreme
774 precipitation expected in Europe and North America from extratropical cyclones.

- 775 *Environmental Research Letters*, 13(12). <https://doi.org/10.1088/1748-9326/aaed59>
- 776 Hochman, A., Harpaz, T., Saaroni, H., & Alpert, P. (2018). The seasons' length in 21st century
777 CMIP5 projections over the eastern Mediterranean. *International Journal of Climatology*,
778 (December 2017), 1–11. <https://doi.org/10.1002/joc.5448>
- 779 Israel, A. of. (2011). *The new Atlas of Israel: the national atlas*. Jerusalem: Survey of Israel ; The
780 Hebrew University of Jerusalem.
- 781 Kahana, R., Ziv, B., Enzel, Y., & Dayan, U. (2002). Synoptic climatology of major floods in the
782 Negev Desert, Israel. *International Journal of Climatology*, 22(7), 867–882.
783 <https://doi.org/10.1002/joc.766>
- 784 Kawase, H., Yoshikane, T., Hara, M., Kimura, F., Yasunari, T., Ailikun, B., et al. (2009).
785 Intermodel variability of future changes in the Baiu rainband estimated by the pseudo global
786 warming downscaling method. *Journal of Geophysical Research Atmospheres*, 114(24), 1–
787 14. <https://doi.org/10.1029/2009JD011803>
- 788 Keller, M., Kröner, N., Fuhrer, O., Lüthi, D., Schmidli, J., Stengel, M., et al. (2018). The
789 sensitivity of alpine summer convection to surrogate climate change: An intercomparison
790 between convection-parameterizing and convection-resolving models. *Atmospheric
791 Chemistry and Physics*, 18(8), 5253–5264. <https://doi.org/10.5194/acp-18-5253-2018>
- 792 Kendon, E. J., Roberts, N. M., Fowler, H. J., Roberts, M. J., Chan, S. C., & Senior, C. A. (2014).
793 Heavier summer downpours with climate change revealed by weather forecast resolution
794 model. *Nature Climate Change*, 4(7), 570–576. <https://doi.org/10.1038/nclimate2258>
- 795 Kendon, E. J., Blenkinsop, S., & Fowler, H. J. (2018). When will we detect changes in short-
796 duration precipitation extremes? *Journal of Climate*, 31(7), 2945–2964.
797 <https://doi.org/10.1175/JCLI-D-17-0435.1>
- 798 Kendon, E. J., Prein, A. F., Senior, C. A., & Stirling, A. (2021). Challenges and outlook for
799 convection-permitting climate modelling. *Philosophical Transactions of the Royal Society
800 A: Mathematical, Physical and Engineering Sciences*.
801 <https://doi.org/10.1098/rsta.2019.0547>
- 802 Krichak, S. O., Tsidulko, M., & Alpert, P. (2000). November 2, 1994, severe storms in the
803 southeastern Mediterranean. *Atmospheric Research*, 53(1–3), 45–62.
804 [https://doi.org/10.1016/S0169-8095\(99\)00045-9](https://doi.org/10.1016/S0169-8095(99)00045-9)
- 805 Kushnir, Y., Dayan, U., Ziv, B., Morin, E., & Enzel, Y. (2017). Climate of the Levant:
806 Phenomena and Mechanisms. In Y. Enzel & B.-Y. Ofer (Eds.), *Quaternary of the Levant:
807 Environments, Climate Change, and Humans* (pp. 31–44). Cambridge, UK: Cambridge
808 University Press.
- 809 Li, J., Wasko, C., Johnson, F., Evans, J. P., & Sharma, A. (2018). Can Regional Climate
810 Modeling Capture the Observed Changes in Spatial Organization of Extreme Storms at
811 Higher Temperatures? *Geophysical Research Letters*, 45(9), 4475–4484.
812 <https://doi.org/10.1029/2018GL077716>
- 813 Lochbihler, K., Lenderink, G., & Siebesma, A. P. (2017). The spatial extent of rainfall events
814 and its relation to precipitation scaling. *Geophysical Research Letters*, 44(16), 8629–8636.
815 <https://doi.org/10.1002/2017GL074857>

- 816 Lochbihler, K., Lenderink, G., & Siebesma, A. P. (2019). Response of Extreme Precipitating
817 Cell Structures to Atmospheric Warming. *Journal of Geophysical Research: Atmospheres*,
818 *124*(13), 6904–6918. <https://doi.org/10.1029/2018JD029954>
- 819 Loft, R. (2020). Earth system modeling must become more energy efficient. *Eos*.
820 <https://doi.org/10.1029/2020EO147051>
- 821 Marra, F., & Morin, E. (2015). Use of radar QPE for the derivation of Intensity–Duration–
822 Frequency curves in a range of climatic regimes. *Journal of Hydrology*, *531*, 427–440.
823 <https://doi.org/10.1016/j.jhydrol.2015.08.064>
- 824 Marra, F., & Morin, E. (2018). Autocorrelation structure of convective rainfall in semiarid-arid
825 climate derived from high-resolution X-Band radar estimates. *Atmospheric Research*,
826 *200*(September 2017), 126–138. <https://doi.org/10.1016/j.atmosres.2017.09.020>
- 827 Marra, F., Zoccatelli, D., Armon, M., & Morin, E. (2019). A simplified MEV formulation to
828 model extremes emerging from multiple nonstationary underlying processes. *Advances in*
829 *Water Resources*, *127*, 280–290. <https://doi.org/10.1016/j.advwatres.2019.04.002>
- 830 Marra, F., Armon, M., Adam, O., Zoccatelli, D., Gazal, O., Garfinkel, C. I., et al. (2021).
831 Towards narrowing uncertainty in future projections of local extreme precipitation.
832 *Geophysical Research Letters*, *Accepted*.
- 833 Meredith, E. P., Ulbrich, U., & Rust, H. W. (2020). Subhourly rainfall in a convection-permitting
834 model. *Environmental Research Letters*, *15*(3). <https://doi.org/10.1088/1748-9326/ab6787>
- 835 Morin, E. (2011). To know what we cannot know: Global mapping of minimal detectable
836 absolute trends in annual precipitation. *Water Resources Research*, *47*(7), 1–9.
837 <https://doi.org/10.1029/2010WR009798>
- 838 Morrison, A., Villarini, G., Zhang, W., & Scoccimarro, E. (2019). Projected changes in extreme
839 precipitation at sub-daily and daily time scales. *Global and Planetary Change*, *182*(May),
840 103004. <https://doi.org/10.1016/j.gloplacha.2019.103004>
- 841 Moustakis, Y., Papalexiou, S. M., Onof, C. J., & Paschalis, A. (2021). Seasonality, Intensity, and
842 Duration of Rainfall Extremes Change in a Warmer Climate. *Earth's Future*, *9*(3), 1–15.
843 <https://doi.org/10.1029/2020EF001824>
- 844 Myhre, G., Alterskjær, K., Stjern, C. W., Hodnebrog, Marelle, L., Samset, B. H., et al. (2019).
845 Frequency of extreme precipitation increases extensively with event rareness under global
846 warming. *Scientific Reports*, *9*(1), 1–10. <https://doi.org/10.1038/s41598-019-52277-4>
- 847 Nasta, P., Adane, Z., Lock, N., Houston, A., & Gates, J. B. (2018). Links between episodic
848 groundwater recharge rates and rainfall events classified according to stratiform-convective
849 storm scoring: A plot-scale study in eastern Nebraska. *Agricultural and Forest*
850 *Meteorology*, *259*(February), 154–161. <https://doi.org/10.1016/j.agrformet.2018.05.003>
- 851 Nerini, D., Besic, N., Sideris, I., Germann, U., & Foresti, L. (2017). A non-stationary stochastic
852 ensemble generator for radar rainfall fields based on the short-space Fourier transform.
853 *Hydrology and Earth System Sciences*, *21*(6), 2777–2797. <https://doi.org/10.5194/hess-21-2777-2017>
- 855 O’Gorman, P. A. (2015). Precipitation Extremes Under Climate Change. *Current Climate*
856 *Change Reports*, *1*(2), 49–59. <https://doi.org/10.1007/s40641-015-0009-3>

- 857 Peleg, N., & Morin, E. (2012). Convective rain cells: Radar-derived spatiotemporal
858 characteristics and synoptic patterns over the eastern Mediterranean. *Journal of*
859 *Geophysical Research: Atmospheres*, 117(15), 1–17. <https://doi.org/10.1029/2011JD017353>
- 860 Peleg, N., Ben-Asher, M., & Morin, E. (2013). Radar subpixel-scale rainfall variability and
861 uncertainty: Lessons learned from observations of a dense rain-gauge network. *Hydrology*
862 *and Earth System Sciences*, 17(6), 2195–2208. <https://doi.org/10.5194/hess-17-2195-2013>
- 863 Peleg, N., Bartov, M., & Morin, E. (2014). CMIP5-predicted climate shifts over the East
864 Mediterranean: Implications for the transition region between Mediterranean and semi-arid
865 climates. *International Journal of Climatology*, 2153(July 2014), 2144–2153.
866 <https://doi.org/10.1002/joc.4114>
- 867 Peleg, N., Marra, F., Faticchi, S., Molnar, P., Morin, E., Sharma, A., & Burlando, P. (2018).
868 Intensification of convective rain cells at warmer temperatures observed from high-
869 resolution weather radar data. *Journal of Hydrometeorology*, JHM-D-17-0158.1.
870 <https://doi.org/10.1175/JHM-D-17-0158.1>
- 871 Pfahl, S., O’Gorman, P. A., & Fischer, E. M. (2017). Understanding the regional pattern of
872 projected future changes in extreme precipitation. *Nature Climate Change*, 7(6), 423–427.
873 <https://doi.org/10.1038/nclimate3287>
- 874 Picard, L., & Mass, C. (2017). The sensitivity of orographic precipitation to flow direction: An
875 idealized modeling approach. *Journal of Hydrometeorology*, 18(6), 1673–1688.
876 <https://doi.org/10.1175/JHM-D-16-0209.1>
- 877 Pichelli, E., Coppola, E., Sobolowski, S., Ban, N., Giorgi, F., Stocchi, P., et al. (2021). The first
878 multi-model ensemble of regional climate simulations at kilometer-scale resolution part 2:
879 historical and future simulations of precipitation. *Climate Dynamics*, 56(11–12), 3581–
880 3602. <https://doi.org/10.1007/s00382-021-05657-4>
- 881 Poujol, B., Prein, A. F., & Newman, A. J. (2020). Kilometer-scale modeling projects a tripling of
882 Alaskan convective storms in future climate. *Climate Dynamics*, (0123456789).
883 <https://doi.org/10.1007/s00382-020-05466-1>
- 884 Prein, A. F., Langhans, W., Fosser, G., Ferrone, A., Ban, N., Goergen, K., et al. (2015). A review
885 on regional convection-permitting climate modeling: Demonstrations, prospects, and
886 challenges. *Reviews of Geophysics*, 53(2), 323–361. <https://doi.org/10.1002/2014RG000475>
- 887 Prein, A. F., Rasmussen, R. M., Ikeda, K., Liu, C., Clark, M. P., & Holland, G. J. (2017). The
888 future intensification of hourly precipitation extremes. *Nature Climate Change*, 7(1), 48–52.
889 <https://doi.org/10.1038/nclimate3168>
- 890 Rasmussen, R., Liu, C., Ikeda, K., Gochis, D., Yates, D., Chen, F., et al. (2011). High-resolution
891 coupled climate runoff simulations of seasonal snowfall over Colorado: A process study of
892 current and warmer climate. *Journal of Climate*, 24(12), 3015–3048.
893 <https://doi.org/10.1175/2010JCLI3985.1>
- 894 Raveh-Rubin, S., & Wernli, H. (2016). Large-scale wind and precipitation extremes in the
895 Mediterranean: dynamical aspects of five selected cyclone events. *Quarterly Journal of the*
896 *Royal Meteorological Society*, 142(701), 3097–3114. <https://doi.org/10.1002/qj.2891>
- 897 Rinat, Y., Marra, F., Armon, M., Metzger, A., Levi, Y., Khain, P., et al. (2020).

- 898 Hydrometeorological analysis and forecasting of a 3-day flash-flood-triggering desert
899 rainstorm. *Natural Hazards and Earth System Sciences Discussions*, 2020, 1–35.
900 <https://doi.org/10.5194/nhess-2020-189>
- 901 Romine, G. S., Schwartz, C. S., Snyder, C., Anderson, J. L., & Weisman, M. L. (2013). Model
902 Bias in a Continuously Cycled Assimilation System and Its Influence on Convection-
903 Permitting Forecasts. *Monthly Weather Review*, 141(4), 1263–1284.
904 <https://doi.org/10.1175/MWR-D-12-00112.1>
- 905 Rostkier-Edelstein, D., Liu, Y., Wu, W., Kunin, P., Givati, A., & Ge, M. (2014). Towards a high-
906 resolution climatology of seasonal precipitation over Israel. *International Journal of*
907 *Climatology*, 34(6), 1964–1979. <https://doi.org/10.1002/joc.3814>
- 908 Rubin, S., Ziv, B., & Paldor, N. (2007). Tropical Plumes over Eastern North Africa as a Source
909 of Rain in the Middle East. *Monthly Weather Review*, 135(12), 4135–4148.
910 <https://doi.org/10.1175/2007MWR1919.1>
- 911 Samuels, R., Rimmer, A., & Alpert, P. (2009). Effect of extreme rainfall events on the water
912 resources of the Jordan River. *Journal of Hydrology*, 375(3–4), 513–523.
913 <https://doi.org/10.1016/j.jhydrol.2009.07.001>
- 914 Samuels, R., Hochman, A., Baharad, A., Givati, A., Levi, Y., Yosef, Y., et al. (2017). Evaluation
915 and projection of extreme precipitation indices in the Eastern Mediterranean based on
916 CMIP5 multi-model ensemble. *International Journal of Climatology*.
917 <https://doi.org/10.1002/joc.5334>
- 918 Sato, T., Kimura, F., & Kitoh, A. (2007). Projection of global warming onto regional
919 precipitation over Mongolia using a regional climate model. *Journal of Hydrology*, 333(1),
920 144–154. <https://doi.org/10.1016/j.jhydrol.2006.07.023>
- 921 Schär, C., Frei, C., Lüthi, D., & Davies, H. C. (1996). Surrogate climate-change scenarios for
922 regional climate models. *Geophysical Research Letters*, 23(6), 669–672.
923 <https://doi.org/10.1029/96GL00265>
- 924 Schwartz, C. S., Romine, G. S., Sobash, R. A., Fossell, K. R., & Weisman, M. L. (2015).
925 NCAR's Experimental Real-Time Convection-Allowing Ensemble Prediction System.
926 *Weather and Forecasting*, 30(6), 1645–1654. <https://doi.org/10.1175/WAF-D-15-0103.1>
- 927 Shepherd, T. G. (2014). Atmospheric circulation as a source of uncertainty in climate change
928 projections. *Nature Geoscience*, 7(10), 703–708. <https://doi.org/10.1038/NGEO2253>
- 929 Shepherd, T. G. (2019). Storyline approach to the construction of regional climate change
930 information. *Proceedings of the Royal Society A: Mathematical, Physical and Engineering*
931 *Sciences*, 475(2225). <https://doi.org/10.1098/rspa.2019.0013>
- 932 Shmilovitz, Y., Marra, F., Wei, H., Argaman, E., Nearing, M., Goodrich, D., et al. (2021).
933 Frequency analysis of storm-scale soil erosion and characterization of extreme erosive
934 events by linking the DWEPP model and a stochastic rainfall generator. *Science of the Total*
935 *Environment*, 787, 147609. <https://doi.org/10.1016/j.scitotenv.2021.147609>
- 936 Sillmann, J., Shepherd, T. G., van den Hurk, B., Hazeleger, W., Martius, O., Slingo, J., &
937 Zscheischler, J. (2021). Event-Based Storylines to Address Climate Risk. *Earth's Future*,
938 9(2), 1–6. <https://doi.org/10.1029/2020EF001783>

- 939 Tarasova, L., Merz, R., Kiss, A., Basso, S., Blöschl, G., Merz, B., et al. (2019). Causative
940 classification of river flood events. *WIREs Water*, 6(4), 1–23.
941 <https://doi.org/10.1002/wat2.1353>
- 942 Taylor, K. E., Stouffer, R. J., & Meehl, G. A. (2012). An overview of CMIP5 and the experiment
943 design. *Bulletin of the American Meteorological Society*. [https://doi.org/10.1175/BAMS-D-](https://doi.org/10.1175/BAMS-D-11-00094.1)
944 [11-00094.1](https://doi.org/10.1175/BAMS-D-11-00094.1)
- 945 Taylor, R. G., Todd, M. C., Kongola, L., Maurice, L., Nahozya, E., Sanga, H., & Macdonald, A.
946 M. (2013). Evidence of the dependence of groundwater resources on extreme rainfall in
947 East Africa. *Nature Climate Change*, 3(4), 374–378. <https://doi.org/10.1038/nclimate1731>
- 948 Tebaldi, C., & Knutti, R. (2007). The use of the multi-model ensemble in probabilistic climate
949 projections. *Philosophical Transactions of the Royal Society A: Mathematical, Physical and*
950 *Engineering Sciences*, 365(1857), 2053–2075. <https://doi.org/10.1098/rsta.2007.2076>
- 951 Trenberth, K. E., Fasullo, J. T., & Shepherd, T. G. (2015). Attribution of climate extreme events.
952 *Nature Climate Change*, 5(8), 725–730. <https://doi.org/10.1038/nclimate2657>
- 953 Tubi, A., Dayan, U., & Lensky, I. M. (2017). Moisture transport by tropical plumes over the
954 Middle East: a 30-year climatology. *Quarterly Journal of the Royal Meteorological Society*,
955 *143*(709), 3165–3176. <https://doi.org/10.1002/qj.3170>
- 956 De Vries, A. J., Tyrlis, E., Edry, D., Krichak, S. O., Steil, B., & Lelieveld, J. (2013). Extreme
957 precipitation events in the Middle East: Dynamics of the Active Red Sea Trough. *Journal of*
958 *Geophysical Research: Atmospheres*, 118(13), 7087–7108.
959 <https://doi.org/10.1002/jgrd.50569>
- 960 Warner, T. T. (2011). *Numerical Weather and Climate Prediction*.
961 <https://doi.org/10.1017/CBO9780511763243>
- 962 Wasko, C., Sharma, A., & Westra, S. (2016). Reduced spatial extent of extreme storms at higher
963 temperatures. *Geophysical Research Letters*, 43(8), 4026–4032.
964 <https://doi.org/10.1002/2016GL068509>
- 965 Westra, S., Fowler, H. J., Evans, J. P., Alexander, L. V., Berg, P., Johnson, F., et al. (2014).
966 Future changes to the intensity and frequency of short-duration extreme rainfall. *Reviews of*
967 *Geophysics*, 52, 522–555. <https://doi.org/10.1002/2014RG000464>
- 968 Zappa, G., Hawcroft, M. K., Shaffrey, L., Black, E., & Brayshaw, D. J. (2015). Extratropical
969 cyclones and the projected decline of winter Mediterranean precipitation in the CMIP5
970 models. *Climate Dynamics*, 45(7–8), 1727–1738. [https://doi.org/10.1007/s00382-014-2426-](https://doi.org/10.1007/s00382-014-2426-8)
971 [8](https://doi.org/10.1007/s00382-014-2426-8)
- 972 Ziv, B., Dayan, U., Kushnir, Y., Roth, C., & Enzel, Y. (2006). Regional and global atmospheric
973 patterns governing rainfall in the southern Levant. *International Journal of Climatology*,
974 *26*(1), 55–73. <https://doi.org/10.1002/joc.1238>
- 975